Title

Structures of the intermediates of Kok's photosynthetic water oxidation clock

Journal

Nature, 563(7731)

ISSN

0028-0836

Authors

Kern, Jan

Chatterjee, Ruchira

Young, Iris D

et al.

Publication Date

2018-11-01

DOI

10.1038/s41586-018-0681-2

Peer reviewed

Structures of the intermediates of Kok's photosynthetic water oxidation clock

Jan Kern[1], Ruchira Chatterjee[1‡], Iris D. Young[1‡], Franklin D. Fuller[1‡], Louise Lassalle[1], Mohamed Ibrahim[2], Sheraz Gul[1], Thomas Fransson[3#], Aaron S. Brewster[1], Roberto Alonso-Mori[4], Rana Hussein[2], Miao Zhang[2], Lacey Douthit[1], Casper de Lichtenberg[5,6], Mun Hon Cheah[6], Dmitry Shevela[5], Julia Wersig[2], Ina Seufert[2], Dimosthenis Sokaras[7], Ernest Pastor[1], Clemens Weninger[4], Thomas Kroll[7], Raymond G. Sierra[4], Pierre Aller[8], Agata Butryn[8], Allen M. Orville[8], Mengning Liang[4], Alexander Batyuk[4], Jason E. Koglin[4], Sergio Carbajo[4], Sébastien Boutet[4], Nigel W. Moriarty[1], James M. Holton[1,7,9], Holger Dobbek[2], Paul D. Adams[1,10], Uwe Bergmann[3], Nicholas K. Sauter[1], Athina Zouni[2*], Johannes Messinger[5,6*], Junko Yano[1*], Vittal K. Yachandra[1*]

[1]Molecular Biophysics and Integrated Bioimaging Division, Lawrence Berkeley National Laboratory, Berkeley, CA 94720, USA.

[2]Institut für Biologie, Humboldt-Universität zu Berlin, D-10099 Berlin, Germany.

[3]Stanford PULSE Institute, SLAC National Accelerator Laboratory, Menlo Park, CA 94025, USA.

[4]LCLS, SLAC National Accelerator Laboratory, Menlo Park, CA 94025, USA.

[5]Institutionen för Kemi, Kemiskt Biologiskt Centrum, Umeå Universitet, SE 90187 Umeå, Sweden.

[6]Department of Chemistry - Ångström, Molecular Biomimetics, Uppsala University, SE 75237 Uppsala, Sweden.

[7]SSRL, SLAC National Accelerator Laboratory, Menlo Park, CA 94025, USA.

[8]Diamond Light Source Ltd, Harwell Science and Innovation Campus, Didcot, Oxfordshire OX11 0DE, UK.

[9]Department of Biochemistry and Biophysics, University of California, San Francisco, CA, 94158, USA

[10]Department of Bioengineering, University of California Berkeley, Berkeley, CA 94720.

[‡]These authors contributed equally to the manuscript.

[*]Corresponding authors.

[#]Present address: Interdisciplinary Center for Scientific Computing, University of Heidelberg, Im Neuenheimer Feld 205, 69120 Heidelberg, Germany

Inspired by the period-four oscillation in flash-induced oxygen evolution of photosystem II (PS II) discovered by Pierre Joliot in 1969, Bessel Kok performed additional experiments and proposed a five-state kinetic model for photosynthetic oxygen evolution, known as Kok's S-state clock or cycle[1,2]. The model comprises four (meta)stable intermediates (S_0, S_1, S_2 and S_3) and one transient S_4 state, which precedes dioxygen formation occurring in a concerted reaction from two water-derived oxygens bound at an oxo-bridged tetra manganese calcium (Mn_4CaO_5) cluster in the oxygen evolving complex (OEC) (reviewed in [3-7]). This reaction is coupled to the two-step reduction and protonation of the mobile plastoquinone Q_B at the acceptor side of PS II (Fig. 1a, Extended Data Fig. 1). Using serial femtosecond X-ray crystallography (SFX) and simultaneous X-ray emission spectroscopy (XES) with multi-flash visible laser excitation at room temperature (RT), we visualize here, for the first time, all (meta)stable states of Kok's cycle by high-resolution structures (2.04-2.08 Å, Extended Data Fig. 1, Extended Data Table 1). In addition, we report structures of two transient states at 150 and 400 µs, revealing important structural changes including the binding of one additional 'water', Ox, during the $S_2 \rightarrow S_3$ state transition (2.20-2.50 Å). Our results suggest direct involvement of one water ligand to calcium (W3) in substrate delivery. The binding of the additional oxygen Ox in the S_3 state between Ca and Mn1 supports O-O bond formation mechanisms involving O5 as one substrate, where Ox is either the other substrate oxygen or is perfectly positioned to refill the O5 position during O_2 release. Thus, our results exclude peroxo-bond formation in the S_3 state, and the nucleophilic attack of W3 onto W2 is unlikely.

All four (meta)stable S-states of PS II were populated by illumination of dark-adapted PS II crystals with 0, 1, 2 or 3 flashes (0F-3F; Fig 1b). The ~2 Å resolution was sufficient for determining the positions of the oxygens bridging the metal atoms, in addition to the terminal water positions of the Mn_4CaO_5 cluster, critical for discriminating between proposed structures of the S-states, unlike previous structures[8,9]. Pivotal for a correct analysis of higher S-state structures is the reliable determination of the S-state composition of the PS II crystals obtained by each flash. We therefore collected the Mn $K\beta_{1,3}$ emission spectra *in situ* (see Methods)[10], simultaneously with diffraction data. The first moment of the $K\beta_{1,3}$ peak shifts toward lower energy in response to the first two flashes (0F→1F→2F) and to higher energy in the 3F sample (Fig. 1c) as expected based on reported Mn redox states (Fig. 1a)[4,11-14]. These data, in combination with *ex situ* O_2 evolution measurements, were used to determine the S-state distribution in each illuminated state (see Methods, Extended Data Fig. 2).

Isomorphous difference maps (F_{obs}-F_{obs}) between the dark and flash-illuminated states at the acceptor side (Fig. 1d-f) indicate a clear period two oscillation of Q_B between its fully oxidized (0F, 2F) and semiquinone $Q_B^{\bullet-}$ (1F) forms. Decrease of the B-factor of the Q_B site after 1F suggests a more tightly bound quinone in the 1F sample, due to the formation of the semiquinone $Q_B^{\bullet-}$. The observation of $Q_B^{\bullet-}$ in the 3F data implies that three electrons were successfully transferred from the Mn_4CaO_5 cluster to the acceptor side, confirming S-state advancement in both PS II monomers ('a' and 'A', Fig. 1d-f, Extended Data Fig. 3).

In the S_1 state, the cluster is in a distinct 'right-open' structure with no bond between Mn1 and O5; the Mn4-O5 distance is ~2.2 Å, while Mn1-O5 is ~2.7 Å (Fig. 2; Extended

Data Table 2), with Mn1 clearly pentacoordinate, and likely in +3 oxidation state[4,11,13-17]. Open, non-cubane structures have been suggested by solution and single crystal polarized EXAFS and EPR data[4,11,15,18].

Upon $S_1 \rightarrow S_2$ transition (1F), one Mn is oxidized from +3 to +4. Fig. 2a shows the electron density map ($2mF_{obs}$-DF_{calc}) of the dark (S_1) and 1F (predominantly S_2) states. The structure of the cluster in the S_2-state remains fundamentally unchanged, with the coordination numbers of all the metals preserved and in accordance with the similarity of the S_1 and S_2 EXAFS spectra[4]. This 'right-open' geometry is consistent with models of the S_2 low spin ($S_{total} = ½$) configuration[19] in which Mn4 is +4. There is no indication of a 'left-open' structure with a O5-Mn1 bond[20]. Only small structural changes are observed in the F_{obs}-F_{obs} difference map in the OEC region, with shifts of Ca, Mn3 and Mn2 and of D1-Asp170 and CP43-Glu354 (Fig. 3a, Extended Data Fig. 4). Interestingly, the strongest difference is observed in the secondary coordination environment, a large negative peak at the location of water W20 (see below).

In Fig. 2a we evaluated the O5 position by overlaying the omit map on the $2mF_{obs}$-DF_{calc} map. In the 0F and 1F data, there is only one envelope of density observed. Upon the $S_2 \rightarrow S_3$ transition (2F) an additional feature appears near Mn1 that can be assigned to an inserted O atom (hydroxo/oxo). In the $2mF_{obs}$-DF_{calc} map of the 2F data, this additional density is visible as a small, but distinct bulge that overlaps with the dominant Mn1 density (Fig. 3b). The presence of this additional density is only distinguishable in the omit map and in the $2mF_{obs}$-DF_{calc} map at high-resolution, and not in the earlier 2.25 Å resolution map (Extended Data Fig. 5)[8].

We refined the 2F data against two partial-occupancy models at the catalytic site based on the S-state populations (see Methods). The S_2-state structure, which is the refined structure for 1F was fixed at 30% in the 2F state. The 2F data were then used to refine the S_3-state structure at 70% occupancy. In the refined S_3 structure, Mn1-Mn4 and Mn1-Mn3 distances are elongated by ~0.2 and ~0.07 Å, respectively, relative to the S_2 structure, and the newly inserted hydroxide or oxo (Ox in Fig. 2a,b), located ~1.8 Å away from Mn1, occupies its 6th coordination site. This change in coordination of Mn1 from penta- to hexa-coordinate is in line with the proposed oxidation of Mn1 from +3 to +4 in the $S_2 \rightarrow S_3$ transition[21-23]. Ox is also bound to Ca (2.50 Å) and it is closer to Ca than is O5 (2.60 Å). The Ca coordination number, however, remains eight, as D1-Glu189, which was ligated to Ca in S_1- and S_2-states (at 2.78 and 2.69 Å, respectively), moves away from Ca in the S_3-state (3.01 Å) making space for Ox (Fig. 2c). These movements are accompanied by changes in the positions of nearby residues (His332, Glu333, His337, Asp342, Ala344, Asp170 of D1, and Glu354, Arg357 of CP43; Extended Data Fig. 4). We note that the current data cannot conclude whether Ox is oxo or hydroxo. However, the position of Ox is compatible with a deprotonated oxo bridge[17].

Suga *et al*.[9] recently reported insertion of an O6 atom at 1.5 Å from O5 in their 2F sample (*ex situ* estimation 46% S_3-state) based on a 2F-0F difference map at 2.35 Å resolution and proposed a peroxide bond formation between O5 and O6 in the S_3-state. The O5-Ox distance of 2.1 Å in our data is ~ 0.6 Å longer than the O5-O6 bond modeled by Suga *et al.* [9], and the location of Ox is 0.9-1.0 Å away from O6. Thus, our data does not agree with the formation of a peroxide-like bond in the S_3 state. We also note that if a peroxide-like bond formation were to occur in the S_3 state, it would have to be

accompanied by the reduction of Mn, which conflicts with various spectroscopic observations[4,15,21] including our current *in situ* XES data (Fig. 1c) that shows oxidation of Mn upon the $S_2 \rightarrow S_3$ transition. We conclude that the differences in interpretation of the data between Suga *et al*.[9] and Young *et al*.[8] arose from the uncertainty when determining oxygen positions at ~2.3 Å resolution, whereas our current data clearly show that Ox is bound to Mn1 and Ca, and that there is no peroxo-bond formation with O5 in the S_3-state.

The third laser flash (3F), advances the highest-oxidized meta-stable S_3-state to the most reduced S_0-state by releasing O_2 and acquiring one water molecule, resetting the catalytic cycle of Kok's clock. The S_0 structure shows the loss of Ox and the return to a motif similar to the dark stable S_1-state (Fig. 2b,c). The decrease of density for Ox in the 3F state (Fig. 2a) is in line with the 60% S_0 population (see Methods).

We collected datasets from two transient states at time points during the $S_2 \rightarrow S_3$ transition, 150 and 400 microseconds after the second flash (Fig. 1b), with resolutions of 2.5 and 2.2 Å, respectively, and computed F_{obs}-F_{obs} maps with the 0F data (Fig. 3, Extended Data Fig. 6, Supplementary Video 1). At the acceptor side, prominent difference peaks are visible in the vicinity of the primary quinone acceptor, Q_A (Fig. 3a) resembling the differences observed at the Q_B site upon formation of $Q_B^{\bullet-}$ 0.2 s after the first flash (see Fig. 1d) and indicating formation of the reduced $Q_A^{\bullet-}$ semiquinone. The same features are visible 250 μs later in the 2F(400μs)-0F difference map, but at reduced intensity. In contrast, the corresponding F_{obs}-F_{obs} difference maps for the datasets collected 0.2 s after the first and second flash do not show any indication of $Q_A^{\bullet-}$ formation, following known kinetics for the $Q_A^{\bullet-}$ formation (sub μs) and decay (on the order of hundreds of μs)[24].

At the OEC, the 2F(150 µs)-0F F_{obs}-F_{obs} map show that the first event after the absorption of the 2nd photon is a movement of Mn4 and Mn1 away from each other by ~ 0.2 Å (Fig. 3b). Density at the Ox site becomes visible in the 2F(400 µs)-0F F_{obs}-F_{obs} map as well as in the 2mF_{obs}-DF_{calc} map, indicating the ligation of Ox to the Mn1 open coordination site. The Ox density (shown in Fig. 3c together with O5 density) increases significantly at 400 µs, and decreases in the 3F data. The remaining Ox density in the 3F data is explained by the ~ 40% S_3 fraction.

In the $S_2 \rightarrow S_3$ transition, a proton transfer followed by electron transfer has been suggested[7,25]. We hypothesize that the proton transfer triggers the shifts of the Mn4 and Mn1 positions in the early stage of the $S_2 \rightarrow S_3$ transition, including shifts of water positions (see below). One option is that W1 deprotonates, while W3 transfers a proton to O5, weakening the O-Mn interaction and allowing the elongation of Mn1 and Mn4[26], necessary for subsequent oxygen insertion at Mn1, which is coupled to a proton transfer from O5 to W1. D1-Tyr161 (Y_Z) is located about 4 Å away from D1-Glu189 and the formation of the positive charge at Y_Z/His189 preceding oxidation of the OEC could trigger these structural changes in its surrounding, inducing a shift of D1-Glu189 away from Ca as observed in the 2F(150µs) data. The subsequent oxidation of Mn1 appears to be directly coupled to the insertion of Ox at the Mn1 open-coordination site observed in the 2F(400 µs) data (Fig. 3b,c). We do not observe the formation of a 'left-open' structure that has been proposed on the basis of DFT-based studies for the early stage of the $S_2 \rightarrow S_3$ transition[20].

The OEC is embedded in an extended network of H-bonds between amino acid residues and waters, connecting it to bulk water and pivotal to its functioning (Fig. 4a,

Extended Data Figure 7, Extended Table 3). We observe several significant changes in this network during the S-state cycle. Movements of the H-bonded water molecules W26-30 (Fig. 4b), of which W26 is located close to O1, indicate that these may be part of a H_2O/H^+ transfer pathway or take part in charge redistributions within the Mn_4CaO_5 cluster during the S-state cycle. W20 is lost in the $S_1 \rightarrow S_2$ transition and reappears during the $S_3 \rightarrow S_0$ transition (Fig. 4c**,** Extended Data Fig. 7, Supplementary Video 2), suggesting that the O4 channel may be used for proton release in the $S_0 \rightarrow S_1$ but not in the $S_2 \rightarrow S_3$ and $S_3 \rightarrow S_0$ transitions. Suga *et al.*[9] did not report S_2-state data, but observed the loss of this water in the 2F data and related it to water insertion during S_3-state formation, which was further reinforced by the proposed computational 'pivot' or 'carousel' mechanisms involving the Mn4 site[20,27]. However, since this water is already absent in S_2 its loss may not have a direct relationship to the formation of S_3.

Additional water position(s) are observed near the Ca-bound W3 in the S_0 structure: W3b at 3.25 Å to Ca has a ~ 60% occupancy in monomer 'A' (Fig. 4d, Extended Data Fig. 7), while the Ca-bound W3 is at 2.59 Å (~ 40%). In monomer 'a', a smaller but similar positive peak is observed in the F_{obs}-F_{calc} map. Therefore, we hypothesize that W3 is the entrance site for the water, which is incorporated into the OEC during the $S_3 \rightarrow S_0$ transition. As indicated by the changes in the Ca ligation environment, W3 may play a similar role in the $S_2 \rightarrow S_3$ transition. We thus suggest that water at the W3 position may act as the entrance site/parking place for either the substrate or the next substrate water in the $S_2 \rightarrow S_3$ and $S_3 \rightarrow S_0$ transitions, in agreement with earlier related suggestions[5,25,28-30]. Possible access routes of water molecules to W3 are shown in Extended Data Fig. 7 (see also Fig. 4a).

Fig. 5 summarizes the structures we determined for all of Kok's S-states and our interpretation of the S-state dependent changes with regard to the mechanism of water oxidation. As outlined above, we propose that the Ox site is filled by W3 during the $S_2 \rightarrow S_3$ transition. The presence of Ox at Mn1 and 2.1 Å away from O5 suggests that Ox either forms the O-O bond with O5 in the $S_3 \rightarrow S_0$ transition (case (i) in Fig. 5), or that Ox is placed between Ca and Mn1 to replace O5 during O_2 formation/release. In the latter case, O-O bond formation may occur between (ii) O5 and W2 or (iii) O5 and W3. We exclude a nucleophilic attack mechanism of W3 or a protein bound water molecule on W2/W1, since the very basis for these suggestions was that the Mn_3CaO_4 cubane of the Mn_4CaO_5 cluster acts as 'battery' by storing oxidizing equivalents, but remains structurally unmodified in a closed cubane geometry[31]. This is in stark contrast to our data that show intricate structural changes in an open cubane involving ligand detachment and the formation of a new Ca-Ox-Mn1 bridge.

Online Content Methods, along with any additional Extended Data display items and Source Data, are available in the online version of the paper; references unique to these sections appear only in the online paper.

Received *; accepted ***.**
Published online *.**

1. Kok, B., Forbush, B. & McGloin, M. Cooperation of charges in photosynthetic O_2 evolution. 1. A linear 4-step mechanism. *Photochem. Photobiol.* **11**, 457-475 (1970).

2. Joliot, P., Barbieri, G. & Chabaud, R. A new model of photochemical centers in system-2. *Photochem. Photobiol.* **10**, 309-329 (1969).

3. Hillier, W. & Wydrzynski, T. ^{18}O-water exchange in photosystem II: Substrate binding and intermediates of the water splitting cycle. *Coord. Chem. Rev.* **252**, 306-317 (2008).

4. Yano, J. & Yachandra, V. K. Mn_4Ca cluster in photosynthesis: Where and how water is oxidized to dioxygen. *Chem. Revs.* **114**, 4175-4205 (2014).

5. Cox, N. & Messinger, J. Reflections on substrate water and dioxygen formation. *Biochim. Biophys. Acta Bioenerg.* **1827**, 1020-1030 (2013).

6. Debus, R. J. FTIR studies of metal ligands, networks of hydrogen bonds, and water molecules near the active site Mn_4CaO_5 cluster in photosystem II. *Biochim. Biophys. Acta Bioenerg.* **1847**, 19-34 (2015).

7. Klauss, A., Haumann, M. & Dau, H. Seven steps of alternating electron and proton transfer in photosystem II water oxidation traced by time-resolved photothermal beam deflection at improved sensitivity. *J. Phys. Chem. B.* **119**, 2677-2689 (2015).

8. Young, I. D. *et al.* Structure of photosystem II and substrate binding at room temperature. *Nature* **540**, 453-457 (2016).

9. Suga, M. *et al.* Light-induced structural changes and the site of O=O bond formation in PSII caught by XFEL. *Nature* **543**, 131-135 (2017).

10. Kern, J. *et al.* Simultaneous femtosecond X-ray spectroscopy and diffraction of photosystem II at room temperature. *Science* **340**, 491-495 (2013).

11. Kulik, L. V., Epel, B., Lubitz, W. & Messinger, J. Electronic structure of the Mn_4O_xCa cluster in the S_0 and S_2 states of the oxygen-evolving complex of photosystem II based on pulse ^{55}Mn-ENDOR and EPR spectroscopy. *J. Am. Chem. Soc.* **129**, 13421-13435 (2007).

12. Dau, H. & Haumann, M. The manganese complex of photosystem II in its reaction cycle—basic framework and possible realization at the atomic level. *Coord. Chem. Rev.* **252**, 273-295 (2008).

13. Peloquin, J. M. *et al.* ^{55}Mn ENDOR of the S_2-state multiline EPR signal of photosystem II: Implications on the structure of the tetranuclear cluster. *J. Am. Chem. Soc.* **122**, 10926-10942 (2000).

14. Krewald, V. *et al.* Metal oxidation states in biological water splitting. *Chem. Sci.* **6**, 1676-1695 (2015).

15. Chernev, P. *et al.* Merging structural information from X-ray crystallography, quantum chemistry, and EXAFS spectra: The oxygen-evolving complex in PSII. *J. Phys. Chem. B.* **120**, 10899-10922 (2016).

16. Tanaka, A., Fukushima, Y. & Kamiya, N. Two different structures of the oxygen-evolving complex in the same polypeptide frameworks of photosystem II. *J. Am. Chem. Soc.* **139**, 1718-1721 (2017).

17. Yamaguchi, K. *et al.* Theory of chemical bonds in metalloenzymes XXI. Possible mechanisms of water oxidation in oxygen evolving complex of photosystem II. *Mol. Phys.* **116**, 717-745 (2018).

18. Yano, J. *et al.* Where water is oxidized to dioxygen: Structure of the photosynthetic Mn_4Ca cluster. *Science* **314**, 821-825 (2006).

19. Pantazis, D. A., Ames, W., Cox, N., Lubitz, W. & Neese, F. Two interconvertible structures that explain the spectroscopic properties of the oxygen-evolving complex of photosystem II in the S_2 state. *Angew. Chem. Int. Edit.* **51**, 9935-9940 (2012).

20. Retegan, M. *et al.* A five-coordinate Mn(IV) intermediate in biological water oxidation: Spectroscopic signature and a pivot mechanism for water binding. *Chem. Sci.* **7**, 72-84 (2016).

21. Dau, H. & Haumann, M. Considerations on the mechanism of photosynthetic water oxidation - dual role of oxo-bridges between Mn ions in (i) redox-potential maintenance and (ii) proton abstraction from substrate water. *Photosynth. Res.* **84**, 325-331 (2005).

22. Cox, N. *et al.* Electronic structure of the oxygen-evolving complex in photosystem II prior to O-O bond formation. *Science* **345**, 804-808 (2014).

23. Siegbahn, P. E. M. Structures and energetics for O_2 formation in photosystem II. *Acc. Chem. Res.* **42**, 1871-1880 (2009).

24. de Wijn, R. & van Gorkom, H. J. Kinetics of electron transfer from Q_A to Q_B in photosystem II. *Biochemistry* **40**, 11912-11922 (2001).

25. Sakamoto, H., Shimizu, T., Nagao, R. & Noguchi, T. Monitoring the reaction process during the S_2 -> S_3 transition in photosynthetic water oxidation using time-resolved infrared spectroscopy. *J. Am. Chem. Soc.* **139**, 2022-2029 (2017).

26. Rossini, E. & Knapp, E.-W. Protonation equilibria of transition metal complexes: From model systems toward the Mn-complex in photosystem II. *Coord. Chem. Rev.* **345**, 16-30 (2017).

27. Askerka, M., Wang, J. M., Vinyard, D. J., Brudvig, G. W. & Batista, V. S. S_3 state of the O_2-evolving complex of photosystem II: Insights from QM/MM, EXAFS, and femtosecond X-ray diffraction. *Biochemistry* **55**, 981-984 (2016).

28. Boussac, A. & Rutherford, A. W. Nature of the inhibition of the oxygen-evolving enzyme of photosystem II induced by NaCl washing and reversed by the addition of Ca^{2+} or Sr^{2+}. *Biochemistry* **27**, 3476-3483 (1988).

29. Tso, J., Sivaraja, M. & Dismukes, G. C. Calcium limits substrate accessibility or reactivity at the manganese cluster in photosynthetic water oxidation. *Biochemistry* **30**, 4734-4739 (1991).

30. Suzuki, H., Sugiura, M. & Noguchi, T. Monitoring the S-state cycle of the photosynthetic water-oxidazing center: Detection of the DOD bending vibration by means of Fourier transform infrared spectroscopy. *Biochemistry* **47**, 11024-11030 (2008).

31. Barber, J. A mechanism for water splitting and oxygen production in photosynthesis. *Nat. Plants* **3**, 17041 (2017).

Supplementary Information is available in the online version of the paper.

Acknowledgments This work was supported by the Director, Office of Science, Office of Basic Energy Sciences (OBES), Division of Chemical Sciences, Geosciences, and Biosciences (CSGB), Department of Energy (DOE) (J.Y., V.K.Y.), by National Institutes of Health (NIH) Grants GM055302 (V.K.Y.), GM110501 (J.Y.) GM126289 (J.K.), GM117126 (N.K.S.), GM124149 and GM124169 (J.M.H.), the Ruth L. Kirschstein National Research Service Award (GM116423-02, F.D.F.), and Human Frontiers Science Project RGP0063/2013 (J.Y., U.B., A.Z.). The DFG-Cluster of Excellence "UniCat" coordinated by T.U. Berlin and Sfb1078, TP A5 (A.Z., H.D.); the Artificial Leaf Project (K&A Wallenberg Foundation 2011.0055) and Vetenskapsrådet (2016-05183) (J.M.); Diamond Light Source, Biotechnology and Biological Sciences Research Council (grant 102593) and a Strategic Award from the Wellcome Trust (A.M.O.) are acknowledged. This research used NERSC, supported by DOE, under Contract No. DE-AC02-05CH11231. Synchrotron facilities at the ALS, Berkeley and SSRL, Stanford, were funded by DOE OBES. SSRL Structural Molecular Biology Program is supported by the DOE OBER, and NIH (P41GM103393). LCLS and SSRL, SLAC National Accelerator Laboratory, are supported by DOE, OBES under Contract No. DE-AC02-76SF00515. We thank the staff at LCLS/SLAC and SSRL (BL 6-2, 7-3) and ALS (BL 5.01, 5.0.2, 8.2.1, 8.3.1).

Author Contributions U.B., V.K.Y. and J.Y. conceived the experiment; R.A.-M., A.Z., J.M., U.B., N.K.S., J.K., V.K.Y., J.Y. designed the experiment; R.C., M.I., L.L., R.H., M.Z., L.D., J.W., I.S., A.Z., J.K. prepared samples; A.Ba., M.L., S.B., R.A.-M., J.E.K.,

S.C. operated the MFX instrument; F.D.F., S.G., E.P., P.A., A.M.O., J.M., J.K. developed, tested and ran sample delivery system; M.H.C., D.Sh., R.C., C.L., J.Y., J.M. performed and analyzed O_2 evolution and EPR measurements; R.C., F.D.F., S.G., M.I., C.L., M.H.C., I.D.Y., A.S.B., R.A.-M., R.H., M.Z., L.L., L.D., D.So., E.P., C.W., T.F., T.K., R.G.S., P.A., A.Bu., A.Ba., M.L., S.B., J.E.K., S.C. A.M.O., A.Z., J.M., U.B., N.K.S., J.K., V.K.Y., J.Y. performed the LCLS experiment; I.D.Y., A.S.B, N.W.M., J.M.H., P.D.A., N.K.S. developed new software for data processing; I.D.Y., A.S.B., L.L, F.D.F., C.W., T.F., P.A., H.D., J.M.H., N.K.S., J.K. processed and analyzed XFEL data; J.M., J.K., V.K.Y., J.Y. wrote the manuscript with input from all authors.

Author Information Reprints and permissions information is available at www.nature.com/reprints. The authors declare no competing financial interests. Correspondence and requests for materials should be addressed to A.Z. (athina.zouni@hu-berlin.de), J.M. (johannes.messinger@kemi.uu.se), J.Y. (jyano@lbl.gov), or V.K.Y. (vkyachandra@lbl.gov).

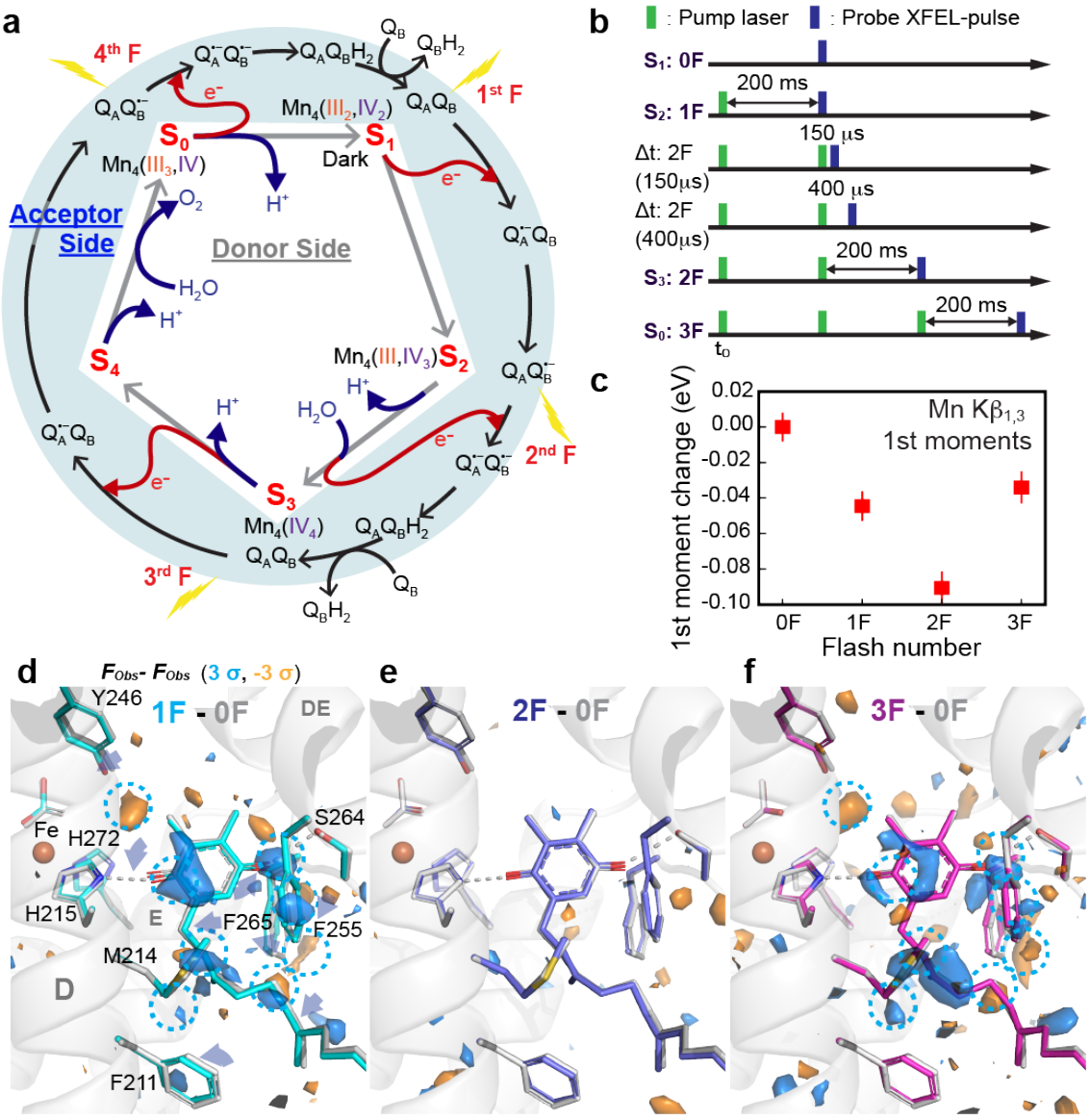

Figure 1 | The oxygen-evolving cycle in photosystem II. a, Relationship between the redox chemistry at the donor (Kok's clock) and acceptor side throughout the oxygen-evolving cycle. **b,** Relative timing of the visible laser (527 nm) pump and X-ray free electron laser for the different illuminated states. **c,** 1st moment change of the Mn $K\beta_{1,3}$ XES spectra from PS II crystals obtained *in situ* simultaneously with the XRD measurements, error bars show SD around mean (see Methods). **d-f,** F_{obs}-F_{obs}

isomorphous difference maps around plastoquinone Q_B contoured at +3 σ (blue) and -3 σ (orange) for the 1F, 2F and 3F states relative to the 0F state. The 0F stick model is shown in light gray, other models have carbons colored cyan (1F), blue (2F) and magenta (3F).

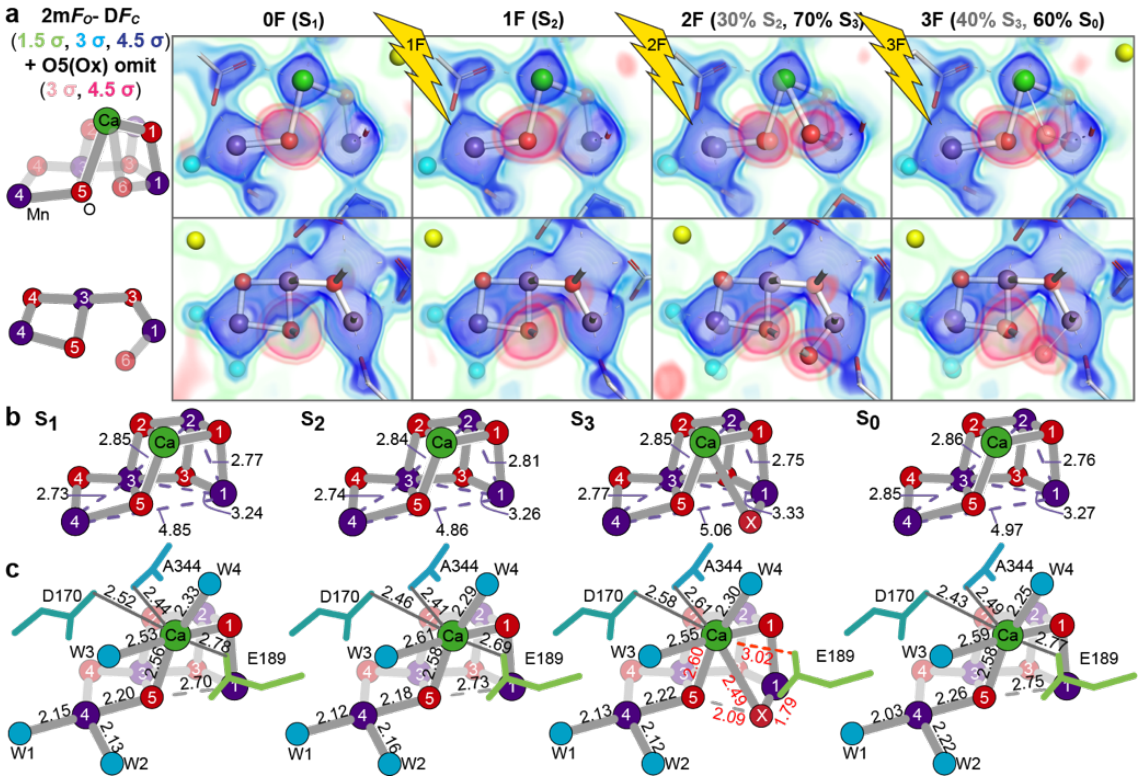

Figure 2 | Stepwise changes at the OEC during the oxygen-evolving Kok cycle. a, Left, labeled diagrams of the OEC atoms in to views. Right: 2mF_o-DF_c density (green to blue) and O5/Ox omit map density (pink) shown as the overlay of several contour levels for the two views of the OEC in the 0F–3F states. The contributions of the S-states to each dataset for the two-component analysis are indicated in parentheses. **b, c,** Atomic distances in the OEC in each S-state in Å, averaged across both monomers. Standard deviations for Metal-metal/metal-bridging oxygen/metal-ligand distances are 0.1/0.15/0.17 Å (see Methods). Ca remains 8-coordinated upon insertion of Ox by detaching D1-Glu189.

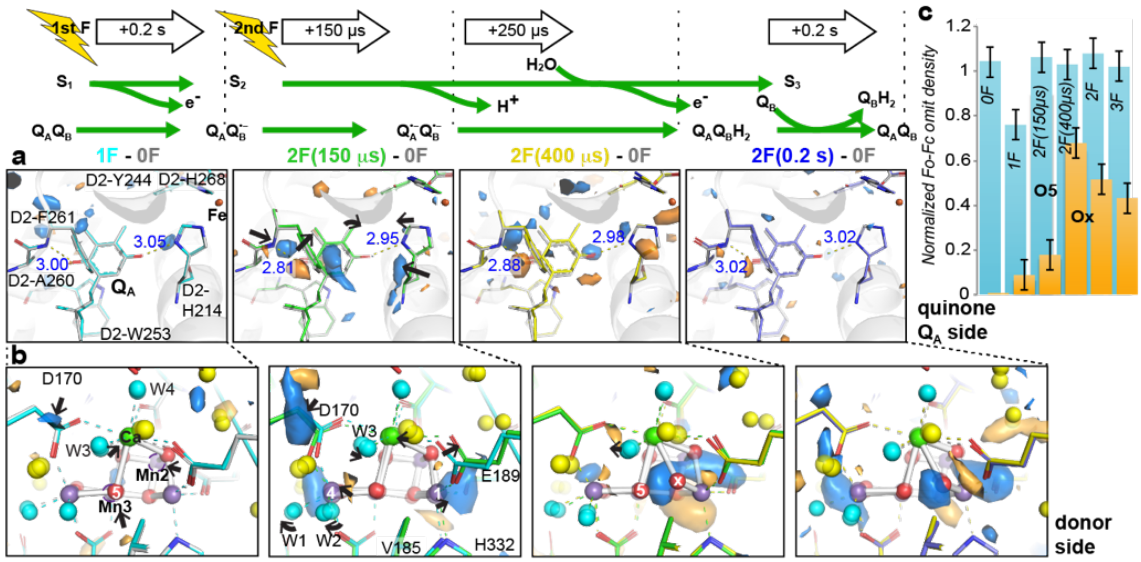

Figure 3 | The $S_2 \rightarrow S_3$ transition in PS II. Isomorphous difference density at (a) quinone Q_A and (b) donor side with the expected reduced state of Q_A at 2F(150us) and less pronounced at 2F(400us), and the oxidation of the OEC and insertion of Ox by 400 µs after the second flash. F_{obs}-F_{obs} difference densities between the various illuminated states and the 0F data are contoured at +3σ (blue) and -3σ (orange), the model for the 0F data is shown in light grey whereas carbons are colored in the models for 1F (cyan), 2F(150 µs) (green), 2F(400 µs) (yellow) and 2F(0.2 s) (blue). **c,** Estimates of occupancies of O5 and Ox based on omit map peak heights normalized against the average electron density maximum at the O2 position in the omit maps. These match full occupancy of O5 throughout and Ox insertion by 400 µs after the second flash. Error bars show SD around mean based on the electron density value at the O2 position (n=12 observations, see Methods).

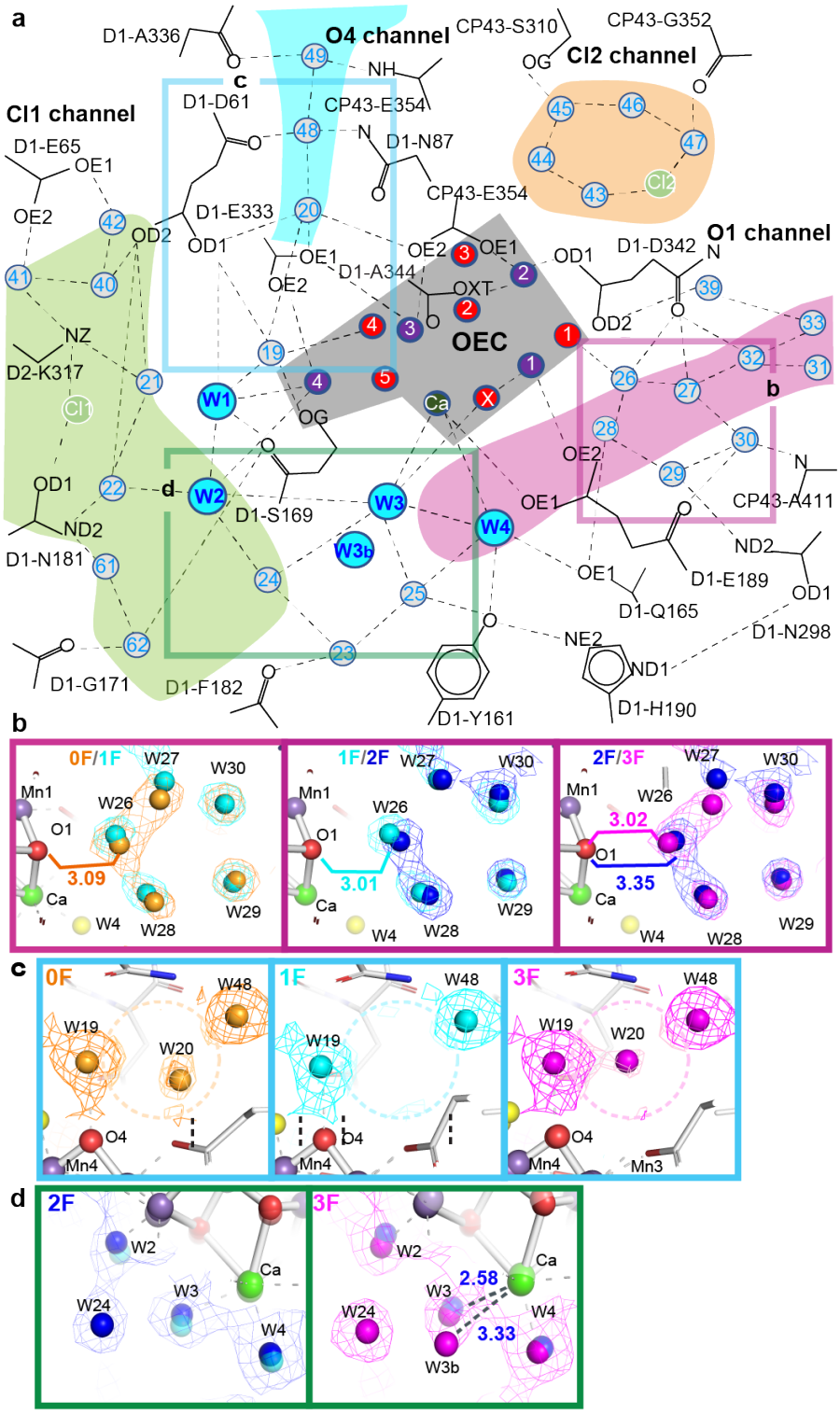

Figure 4 | Water network around the OEC. a, Schematic of the hydrogen bonding network surrounding the OEC with indication of the starting points of channels

connecting the OEC to the solvent-exposed surface of PS II for either possible water movement or proton transfer. **b-d,** Changes in selected water positions between the 0F-3F states overlaid with 2mF_{obs}-DF_{calc} maps in those states contoured at 1.5 σ. Positions in the schematic view are indicated by boxes of the same color. Selected distances are given in Å. **b,** Oscillation of the cluster of five waters next to O1 with the O1-O26 distance alternating long-short-long-short from 0F-3F. **c**, W20 and its direct surrounding are shown indicating disappearance of W20 in the 1F (S_2) data and reappearance in 3F (S_0). **d**, Environment of Ca-bound W3, indicating the presence of a second water position for W3 in the S_0-state (3F).

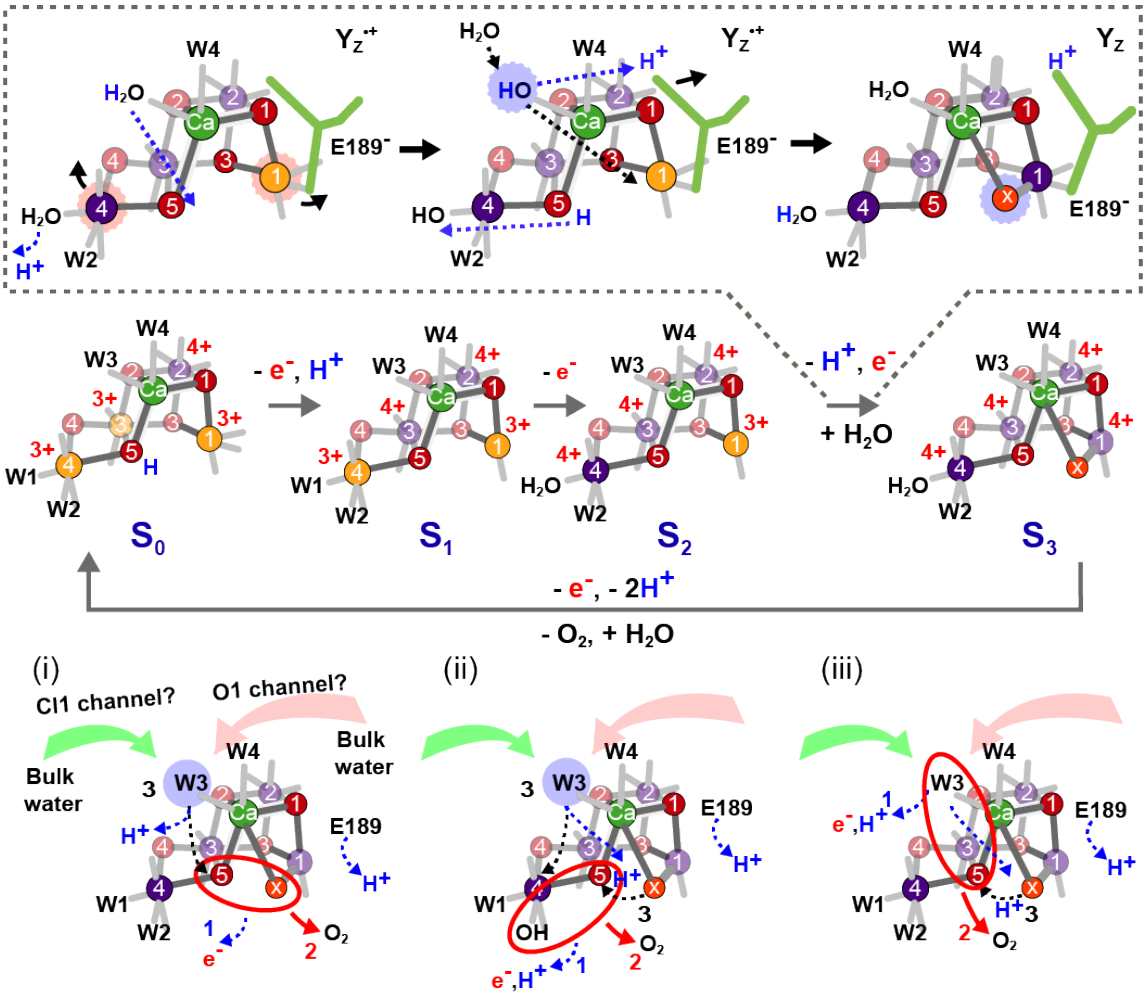

Figure 5 | Schematic structures of the S-states in the Kok cycle of PS II and proposed reaction sequences for O-O bond formation in the S_4 state. The likely position of Mn-oxidation states (Mn^{+3} is depicted in orange, Mn^{+4} in purple) as well as protonation/deprotonation reactions are indicated for each S-state; the proposed steps in the $S_2 \rightarrow S_3$ transition including Ox insertion are indicated in the dashed box with blue arrows signifying atom movements. Three likely options (i, ii, iii) for the final $S_3 \rightarrow S_0$ transition are given in the bottom part, including possible order of 1) electron and proton release; 2) O-O bond formation and O_2 release; 3) refilling of empty substrate site.

Methods

Sample preparation. PS II dimers were extracted and purified from *T. elongatus* as reported previously[32]. PS II crystals ranging in size from 20-60 μm were then prepared using a modified seeding protocol[33]. The crystals were dehydrated by treatment with high concentrations of PEG 5000. The final crystal suspension used for XRD measurements was in 0.1 M MES pH 6.5, 0.1 M ammonium chloride and 35% (w/v) PEG 5000, with ~0.5-0.8 mM chlorophyll concentration. After loading into the sample delivery syringe (Hamilton gastight syringe, 1000 μl), each sample syringe was given a preflash using green LED diodes (525 nm, Thorlabs, USA) to synchronize the samples, ensure that all centers have an oxidized tyrosine D and maximize yield of the higher S-states upon subsequent flashing. The intensity of the light used at the sample for the preflash was 2 μmol $m^{-2}s^{-1}$. The samples were exposed for ten seconds while rotating the syringe, and dark-adapted for 30 minutes to 2 hours after the preflash. We note that the PS II core complexes in our sample preparation contain sufficient number of natural quinones to drive the catalytic reaction through the cycle[8,34,35].

Characterization. *O_2 activity:* Measurement of the O_2 yield by means of a Clark-type electrode under continuous illumination showed the O_2 evolution rate of PS II solution before crystallization is 2300 ± 100 μmol O_2/(mg(Chl) × h) and after crystallization in the final buffer comprising 0.1 M MES pH 6.5, 0.1 M ammonium chloride it is 2100 ± 80 μmol O_2/(mg(Chl) × h) with 0.4 mM PPBQ. ~90% activity is retained after crystallization

EPR measurements: All sample batches used at the LCLS were checked with EPR for S-state turnover and Mn(II) content. The low-temperature X-band EPR spectra were measured using a Varian E109 EPR spectrometer equipped with a Model 102 Microwave bridge. For the turnover measurements, sample temperature was maintained at 8 K using an Air Products LTR liquid helium cryostat. The following spectrometer conditions were used: microwave frequency, 9.22 GHz; field modulation amplitude, 32 G at 100 kHz; microwave power, 20 mW. The turnover in the crystals was characterized using EPR spectroscopy. The turnover of the samples was measured as a function of the multiline EPR signal of the S_2 state, which oscillates with a period of four as a function of flash number. We observed the EPR signal for samples after a single turnover flash (1F) and monitored turnover by following decreases in amplitude of the multiline signal by subsequent flashes. In order to check the Mn(II) content sample temperature was maintained at 20 K and the sensitivity of the measurement allowed to detect the presence of as low as 2% Mn(II) (compared to total Mn content) in the sample. The following spectrometer conditions were used: microwave frequency, 9.22 GHz; field modulation amplitude, 32 G at 100 kHz; microwave power, 1 mW. The Mn (II) content estimated by EPR agreed with that determined by *in situ* XES measurements[36].

MIMS measurements: The S-state advancement of crystals was also evaluated by MIMS (Membrane inlet mass spectroscopy). A crystal suspension with approximately 10% ^{18}O-labelled water was placed in the thin-layer MIMS setup and subjected to a laser preflash before dark adaptation for 40 minutes at room temperature. The sample was then subjected to 2F at 5 Hz frequency and the O_2 yield is detected as a peak at m/z 34. The procedure was repeated for 3F and 4F using new crystal suspensions each time. The O_2 yield pattern as function of flash number were calculated by subtracting the normalized

O_2 yield of a flash number with the yield from the preceding flash number and normalized to 3F. The O_2 pattern can be fitted satisfactorily with an average miss parameter of 22%. The estimated S-state population is presented in Extended Data Fig. 2.

Determination of the S-state population: We evaluated the S-state advancement of PS II crystal suspension by two methods, *in situ* and *ex situ*. X-ray emission spectroscopy that monitors the oxidation state of Mn was collected simultaneously with the XRD data (**Fig. 1c**) as described previously[10,36,37]. The obtained single crystal XES spectra and details about XES data evaluation have been published recently[36]. Standard deviations for the first moments of the XES data shown as error bars in Fig. 1c were determined by random sampling of each of the data sets 1000 times (each time randomly splitting the data into two subsets) and then calculating the standard deviation from the resulting 2000 spectra for each flash state. Further details are given in ref. 38.

Flash-induced oxygen measurements (MIMS) for O_2 detection[38-40] was carried out prior to the XFEL experiment. We have estimated the S-state population from both methods and these are presented in Extended Data Fig 2. For the purpose of refinement of the structural models in the 2F data, we have fixed the S_3 populations to 70% and S_2 to 30%. For the 3F data, we have fixed the S_3 populations to 40%, and fit the remaining 60% as S_0, since S_0 is the major population within the 60%. Further details regarding the refinement of the mixed models in the 2F and 3F data are given below in section "Model building and map calculation".

Sample injection and illumination. The crystallography data were collected at the MFX instrument of LCLS[41,42] during experiments LN84 and LQ39. The Drop-on-Tape (DOT) sample delivery method was used in combination with acoustic droplet ejection (ADE)[37]. For capturing the stable intermediates S_2, S_3, and S_0, each droplet of the crystal suspension was illuminated by 120 ns laser pulses at 527 nm using a Nd:YLF laser (Evolution, Coherent) via fiber-coupled outputs 1, 2 and/or 3, resulting in a delay time of 0.2 s between each illumination, and of 0.2 s between the last illumination and the X-ray probe[37]. We implemented a feedback control system of the belt speed and deposition delay, and the flashing delay and droplet phase where adjusted accordingly[37].

For ex-situ testing of light saturation for the DOT system, a 100-150 μm thick sample film was established with the help of a washer between the silicon membrane of the mass spectrometer inlet and a thin microscope glass plate ('thin layer MIMS setup'). In this experiment, the samples are saturated at 70 mJ/cm^2. The details are described in Young *et al.*[8] At the XFEL, a light intensity of 120±10 mJ/cm^2 was applied.

X-ray diffraction setup and data processing. PS II crystals where measured using X-ray pulses of ~40 fs length at 9.5 keV and with an X-ray spot size at the sample of ~3 μm in diameter. XRD data were collected on a Rayonix MX170 HS detector operating in the 2-by-2 binning mode at its maximum frame rate of 10 Hz. This mode provided the optimal tradeoff of resolving power between adjacent Bragg reflections and quantity of images collected.

We developed the *cctbx.xfel* graphical user interface to track diffraction data acquisition, provide real-time feedback, and submit processing jobs. Processing jobs used *dials.stills_process*, a program within the *cctbx.xfel* framework that carries out lattice

indexing, crystal model refinement, and integration and adopts a variety of defaults suited to XFEL still images[43-48]. For each image, strong spots are first selected. Next, candidate basis vectors describing the lattice of strong spots are identified, and an optional target cell is used to filter these candidates. A crystal model (composed of a unit cell and crystal orientation) is then refined to minimize differences between observed spot centroids and predicted positions, and this model is used to generate a complete set of indexed positions on the frame. Finally, signal at these positions is integrated and any corrections or uncertainties are taken into account. We found that with the stills-specific defaults and very few non-default parameters, 20-50% of shots (which we estimate to be a majority of the shots containing crystals) could be successfully indexed.

The powder diffraction pattern of a silver(I) behenate sample (Alfa Aesar) in a quartz capillary (Hampton Research, 10 μm wall thickness) was used to obtain an initial estimate of detector distance. Initial indexing results were used to refine a detector distance and position for each interval between adjustments to the sample delivery system or detector position. These higher-precision detector positions were used in subsequent indexing and integration trials, resulting in a maximum of four distinct lattices indexed on a single shot.

Cluster.unit_cell, a command line tool in *cctbx* that clusters similar unit cells according to the Andrews-Bernstein distance metric[49,50], was used to obtain the average unit cell. This unit cell was used as the target unit cell when reprocessing all experimental data with *dials.stills_process*.

A total of 1,565,863 integrated lattices were obtained using *dials.stills_process* with a target unit cell of a=117.5 Å, b=222.8 Å, c=309.6 Å, $\alpha=\beta=\gamma=90°$ and the space group $P2_12_12_1$. Signal was integrated to the edges of the detector in anticipation of a per-image resolution cutoff during the merging step. Integrated intensities were corrected for absorption by the Kapton conveyor belt to match the position of the belt and crystals relative to the X-ray beam[37].

Finally, XES data collected simultaneously with the diffraction images were used to sort out and exclude any sample batches that indicate the presence of Mn(II) released during the on site crystallization[36]. It was also used to confirm the advancement of S-states by fiber-coupled lasers and a free space laser.

Image sets were also culled to include only images diffracting beyond 6 Å (for small datasets) or beyond 3 Å (all others), similar to a procedure which has been used previously[51] to improve statistics in large datasets suffering from contamination by low-quality images. Until the experiments described here, we were typically data-limited and have focused data processing methods development on discovering how to extract the most signal from low-multiplicity datasets[52,53]. Several data visualization tools we implemented in the *cctbx.xfel* graphical user interface have made it possible to tune crystallization conditions and the sample delivery system to optimize diffraction quality early in an XFEL diffraction experiment, resulting in collection of much larger quantities of data. Although post-refinement and the per-image resolution cutoffs used in *cxi.merge* downweigh or remove most spot predictions without signal, we still observed improvement in merging statistics and map quality when excluding lattices diffracting to a resolution poorer than 3 Å from these larger datasets, likely because of the limitation in

orientational precision when indexing the small number of reflections visible on low-resolution stills.

The remaining integrated images were merged using *cxi.merge* as described previously[8], with a couple of modifications. The default unit cell outlier rejection mechanism in *cxi.merge* was sufficiently selective on the image set curated as described above, so a pre-filtering step was not necessary. Also, a reference model and dataset with a compatible unit cell — used by *cxi.merge* during scaling — were available from previous beam times, so a preliminary merging step with *PRIME* was not necessary.

Final merged datasets were acquired for the 0F, 1F, 2F(150 μs,) 2F(400 μs), 2F, and 3F states to resolutions between 2.50 and 2.04 Å, containing between 4231 and 30366 images (Extended Data Table 1). Additionally, data from all illuminated states were aggregated, culled to the subset of images extending past 2.2 Å, and merged as a separate 'combined' dataset to 1.98 Å (results not shown).

Model building and map calculation: Initial structure refinement against the 'combined' dataset at 1.98 Å was carried out starting from a previously acquired high-resolution PS II structure in the same unit cell (PDB ID: 5TIS) using *phenix.refine*[54,55]. After an initial rigid body refinement step, *xyz* coordinates and isotropic B-factors were refined for tens of cycles with automatic water placement enabled. Custom bonding restraints were used for the OEC (with large sigma values, to reduce the effect of the strain at the OEC on the coordinate refinement), chlorophyll-*a* (CLA, to allow correct placement of the Mg relative to the plane of the porphyrin ring), and unknown lipid-like ligands (STE). Custom coordination restraints overrode van der Waals repulsion for coordinated chlorophyll Mg atoms, the non-heme iron, and the OEC. Following real space refinement in *Coot*[56] of selected individual sidechains and the PsbO loop region and placement of additional water molecules, the model was refined for several additional cycles with occupancy refinement enabled, then as before without automatic water placement, and then as before with hydrogen atoms. NHQ flips and automatic linking were disabled throughout. A final 'combined' dataset model was obtained with R_{work}/R_{free} of 17.92%/22.01%.

The above model was subsequently refined against the illuminated datasets to produce models differing primarily at the OEC and plastoquinone, as confirmed by isomorphous difference maps, with the lattermost refinement settings and different OEC bonding restraints. OEC bonding restraints for the 0F dataset prevented large deviations from the high-resolution dark state OEC structure reported by Suga *et al.* (PDB ID: 4UB6[53]). Bonding restraints for the other datasets loosely restrained the models to metal-metal distances matching spectroscopic data and metal-oxygen distances matching the most likely proposed models[57-61]. A number of ordered water positions were excluded from subsequent automatic water placement rounds by renaming the residue names to OOO and supplying *Phenix* with a bonding restraint CIF dictionary for OOO identical to that for HOH, and the waters coordinating the OEC were incorporated into the OEC restraint CIF file directly. After 12-15 of cycles of refinement in this manner, individual illuminated states at various resolutions were obtained ranging in R_{work}/R_{free} from 16.69%/24.60% to 19.33%/26.39% (Extended Data Table 1).

After the first cycles of refinement for the 2F data using the initial OEC model from the 0F data as starting point, a positive peak in the mF_{obs}-DF_{calc} density close to Mn1 became visible (see also Extended Data Fig. 5) and the automatic water placement step in refinement placed a water at the OEC between O5 and Mn1. We designated this new water as a potential Ox and added it to the OEC. We tested several different starting positions for this Ox, including a position similar to O6 (Suga *et al.*)[9] at 1.5 Å distance from O5, but refinement resulted in shifts of the Ox away from O5 and close to Mn1. mF_{obs}-DF_{calc} difference maps calculated for different positions of this additional oxygen also confirmed a placement at about 1.8 Å from Mn1 and 2.1 Å from O5. For the final refinement Ox was included in the CIF restraints for the OEC in the S_3 state.

To best approximate the contributions of dimers that did not advance to the next S-state due to illumination misses, for the 2F and 3F datasets, the 2F and 3F models were split into A and B alternate conformers in regions of chains A/a, C/c and D/d surrounding (and including) the OEC. These residues are A55-65, A160-190, A328-344, C328, C354-358, D352. Population of the S_3 and S_0 states in the 2F and 3F data was estimated based on oxygen evolution and XES measurements (Extended Data Fig. 2) and rounded to the nearest 10%, yielding 70% S_3 state population in the 2F dataset and 60% S_0 state population in the 3F dataset. Accordingly, for the 2F dataset, the main conformer across this entire region was set at 0.7 occupancy, and the minor conformer was set at 0.3 occupancy. Analogously, for the 3F dataset, conformers were set at 0.6 and 0.4 to match an estimated 40% contribution from the S_3 state and modeling the remaining 60% as the S_0 state. The major conformer was allowed to refine as usual, while the minor conformer was fixed during refinement and set to match the major conformer of the previous S-state (*e.g.* fixed coordinates for S_2 at 30% for the 2F, S_3-enriched state). This was achieved by least-squares fitting the refined model of the previous S-state onto the new model at the split region in *PyMol*[62] and replacing the minor conformer atomic coordinates with the fitted model coordinates, then excluding the newly placed atoms from refinement in *phenix*.

Although *phenix.refine* supports modeling of three or more conformers, we limited our analysis to two conformers in consideration of both the limits of the resolution and the precision of the S-state contribution estimates, and we did not model a ~10% contribution of the S_1 state in the 1F dataset. When placing the refined S_3 state model into the 3F model at 0.4 occupancy, we used the 0.7 occupancy model refined as described above, not the combination of both conformers. This analysis was not possible for the 2F(150 μs) and 2F(400 μs) models since the complementary components would be time points 150 μs and 400 μs after the S_1 state, structures we have not probed.

Estimated positional precision: The maximum-likelihood coordinate error calculated during refinement is a general-purpose metric for positional error but is subject to several limitations including the impact of bonding, angle, coordination and other restraints on the refined model. Previously, we have generated ballpark estimates of positional error for various sections of the model by setting them to zero occupancy, conducting simulated annealing followed by refinement, placing the same components into omit density, and reporting the final magnitude of the shift between the centers of mass of the original and omit density-fitted components[8]. This is impractical for more than a handful of representative cofactors or segments of the main chain and is difficult for much

smaller groups of atoms or individual atoms whose environments easily fill the missing density region if it is not artificially held open. We also tried multi-start kicked model refinement and found that the oxygen-evolving complex refined back to nearly the same position in all trials. We therefore shifted our focus to a tool that perturbs the structure factors directly. By perturbing structure factors by $\pm|F_{obs} - F_{model}|$ in 100 trials using the *END/RAPID* command line tools, we added noise proportional to the error in the model to generate 100 perturbed datasets for each illumination state, re-refined kicked models against each new dataset, and calculated the mean and standard deviation of selected bond distances across the re-refined models[63]. Metal-metal distances at the OEC had standard deviations between 0.08 and 0.12 Å across these trials, while distances between OEC metals and bridging oxygen atoms had standard deviations varying between 0.10 and 0.23 Å and distances between OEC metals and coordinating ligands were found to have standard deviations between 0.13 and 0.20 Å.

Estimating the uncertainty of the omit densities: Changes of the electron density at the positions of Ox and O5 were obtained from O5 and Ox omit maps and normalized against the average electron density maximum at the O2 position in O2 omit maps, assuming that O2 is always fully occupied in the different flash states. The standard deviation of the electron density value at O2 over all datasets and both monomers was also used to estimate the uncertainty of the normalized omit density. The omit densities of a particular dataset were divided by the average omit densities of the chloride ions of the same dataset to equate the densities from different datasets.

Isomorphous difference maps: Slight, nonphysical differences in merged unit cells were modeled across the illumination states in this sequence of datasets. Large distributions of unit cells derived from indexing with *dials.stills_process* are known to reflect uncertainty in the crystal model, not variation among actual crystals[64], and the distributions also shifted as sample-to-detector distance changed over the course of an LCLS shift. Because it was not possible to cycle through all illumination conditions throughout each of the experiments, the average unit cell dimensions varied across datasets as well, resulting in the aforementioned nonphysical differences in merged unit cells. To obtain isomorphous difference maps without artifacts from these apparent unit cell variations we computed a second set of data, selecting only lattices with unit cells within 1% of the target unit cell. The resulting smaller datasets were at slightly reduced resolution (Extended Data Table 1b). However, because the merged unit cell differences were small, artifact free isomorphous difference maps could be calculated between pairs of these datasets. The corresponding mtz and pdb files for these smaller datasets are available from the authors upon request.

Code availability.

The open source programs *dials.stills_process*, the *cctbx.xfel* GUI and *cxi.merge* are distributed with *DIALS* packages available at http://dials.github.io, with further documentation available at http://cci.lbl.gov/xfel.

Data availability.

The atomic coordinates and structure factors have been deposited in the Protein Data Bank, www.pdb.org (PDB ID code 6DHE for the 0F, 6DHF for the 1F, 6DHO for the 2F, 6DHG for the 2F(150μs), 6DHH for the 2F(400μs) and 6DHP for the 3F data).

Extended Data

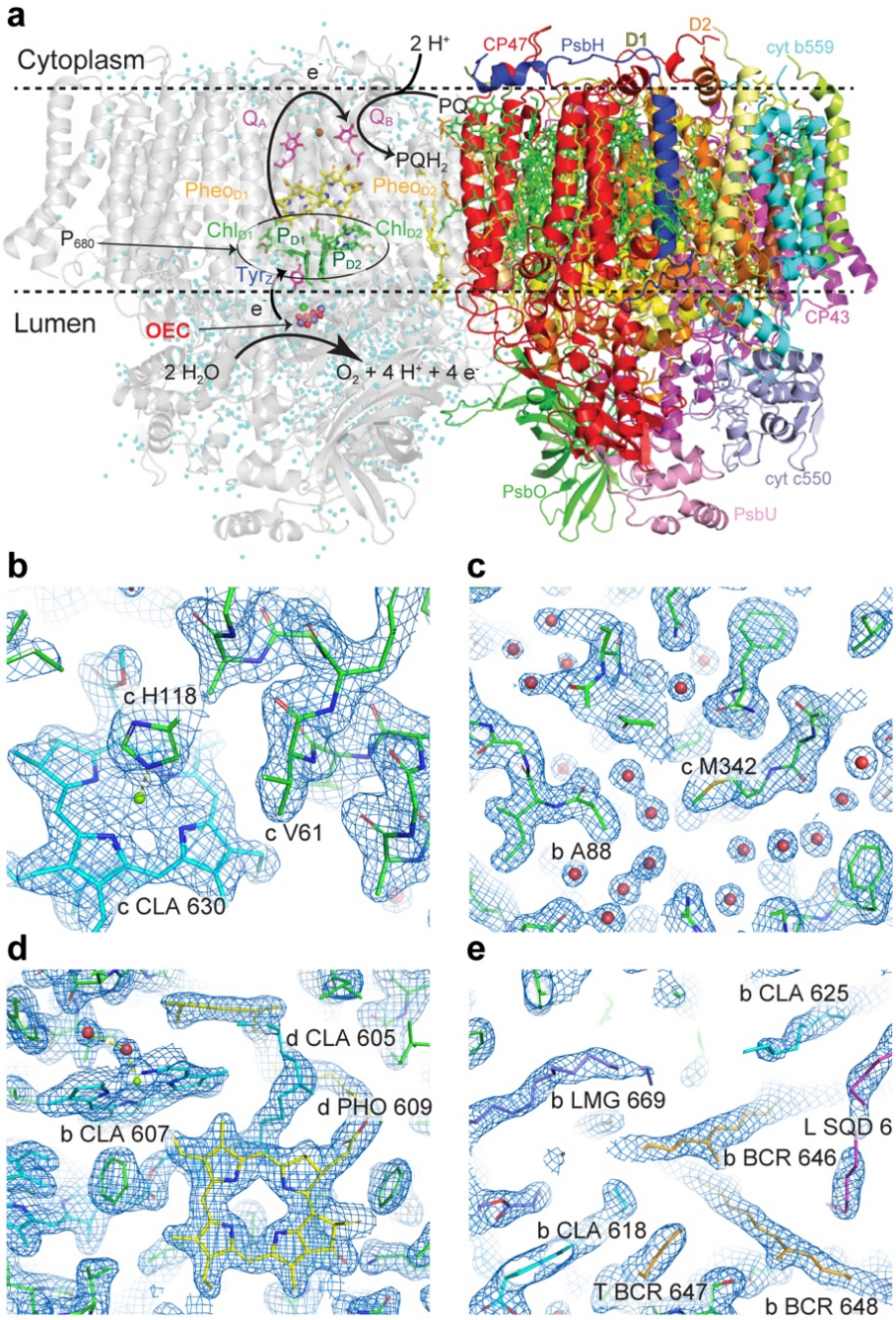

Extended Data Figure 1 | Overview of the PS II structure and electron density maps of the 3F state. a, Structure of the native PS II homodimer. In the left monomer the location of cofactors for the initial charge separation (P_{680}, $Pheo_{D1}$), and for the electron transfer leading to the reduction of the plastoquinone (Q_A, Q_B) at the acceptor side and to the oxidation of the OEC at the donor side by $P680^+$ are indicated. In the right monomer, the locations of the protein subunits are displayed. **b-d,** $2mF_{obs}$-DF_{calc} map (blue, 1.5 σ contour) obtained from the room temperature 3F dataset. **b,** Density around the main

chain and a chlorophyll. **c,** well-resolved ordered water molecules. **d,** Chlorophyll and pheophytin molecules with well-resolved tails. **e,** Clear density in hydrophobic regions and along cofactor hydrocarbon tails.

a

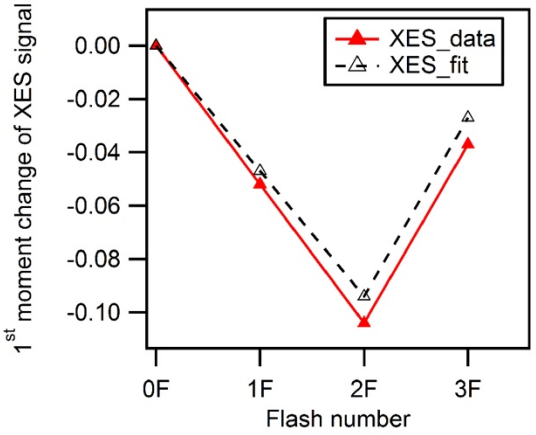

b

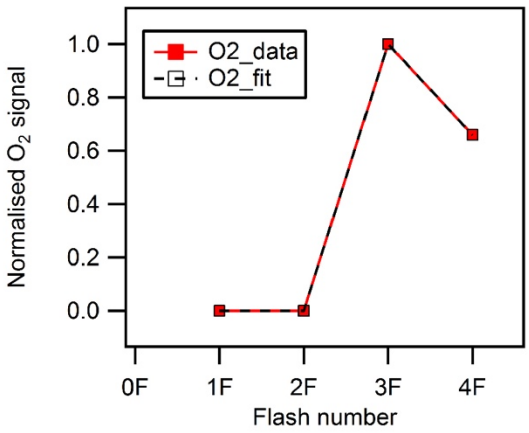

c

Sample	**S_0**		**S_1**		**S_2**		**S_3**	
	XES	O_2	XES	O_2	XES	O_2	XES	O_2
0F	0	0	100	100	0	0	0	0
1F	0	0	8	22	92	78	0	0
2F	0	0	2	5	30	34	68	61
3F	50	48	2	1	5	11	43	40

Extended Data Figure 2 | Flash-induced S-state turnover of PS II micro crystals. a, Change of the first moment of the *in situ* measured Mn Kβ XES as a function of flashes and fit to the data. **b,** Flash induced O_2 yield as measured by MIMS as a function of flash number and fit to the data. **c,** The estimated S-state population (in %) for each of the flash states from fitting of the XES data and of the flash induced O_2 evolution pattern of a suspension of PS II crystals at pH 6.5. Two different fits were performed: a global fit of both O_2 and XES data using an equal miss parameter of 22% and 100% S_1 population in the 0F sample (black traces in panels a and b; S-state distribution listed in the Table columns headed 'O_2') and a direct fit of the XES data using a 8% miss parameter in the $S_1 \rightarrow S_2$ and a 27% miss parameter for the $S_2 \rightarrow S_3$ and $S_3 \rightarrow S_0$ transitions ('XES' in Table). For the XES fit, shifts of -0.06 eV per oxidation state increase for all S-states were assumed. XES raw spectra can be found in ref. [38].

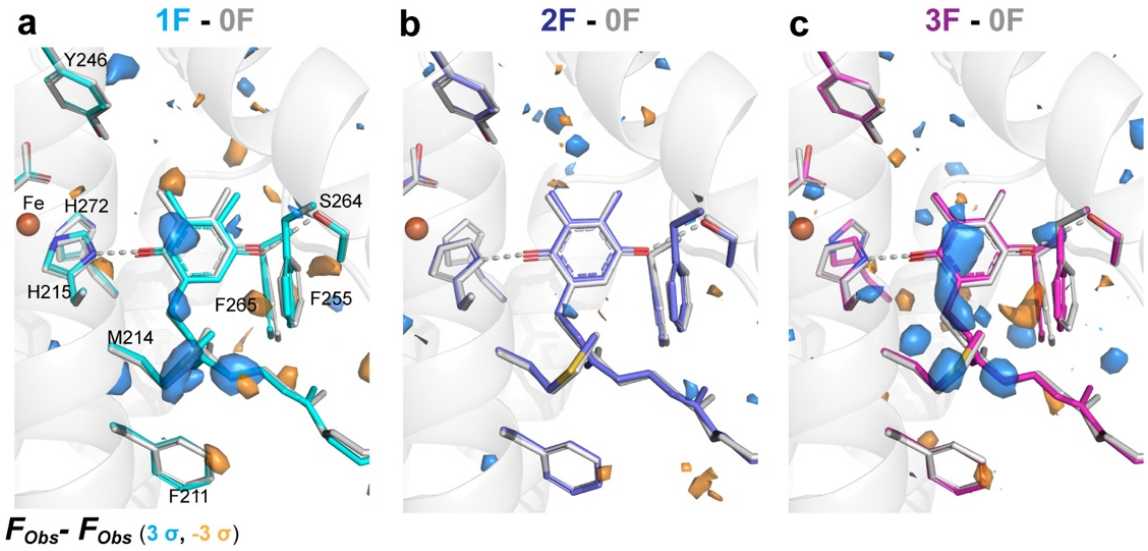

Extended Data Figure 3 | Isomorphous difference maps in the 2nd monomer at the Q_B site. a-c, F_{obs}-F_{obs} maps contoured at 3 σ at plastoquinone Q_B in monomer "a". **a,** 1F-0F difference map matching reduction of the plastoquinone to a semiquinone and concomitant slight geometry change. **b,** 2F-0F difference map matching replacement of the fully reduced quinol with another quinone at the original position. **c,** 3F-0F difference map, showing again structural changes similar to the 1F-0F map, indicating formation of the semiquinone. Similar views are shown for monomer "A" in Fig. 1d-f and comparison of both monomers indicates similar flash induced changes in both monomers.

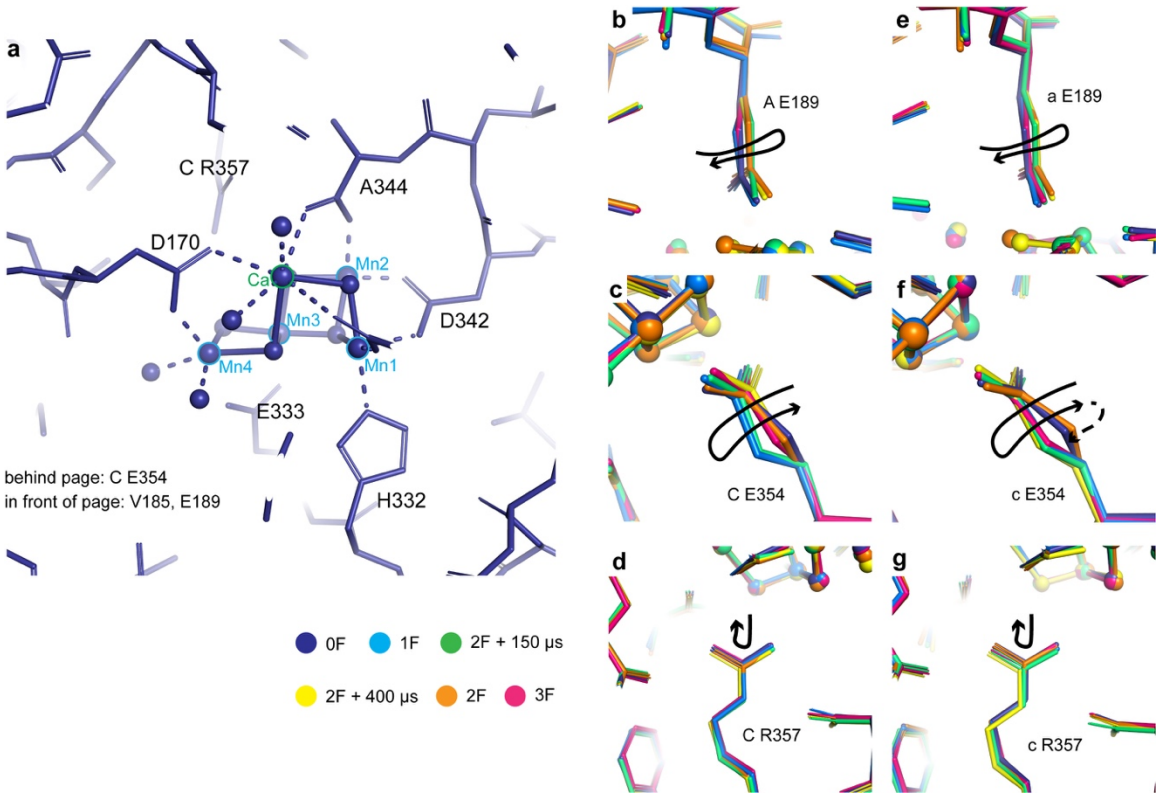

Extended Data Figure 4 | Movement of ligands around the OEC in the different S-states. a, Overview of the ligand environment of the OEC, showing the dark state (0F) structure. Coordination of the OEC by nearby sidechains and water molecules is indicated by dashed lines. **b-g**, Trends for selected individual sidechains in both monomers (b,c,d: monomer 'A'; e,f,g: monomer 'a'). Overlays of the refined models at the OEC following least-squares fitting of subunit D1 residues 55-65, 160-190 and 328, subunit CP43 residues 328 and 354-358, and chain D residue 352 of each other model to the 0F model. Greatest magnitude and most consistent motions of sidechains near the OEC through the sequence of illuminated state models is annotated with arrows indicating the trend. A motion only observed in one monomer is indicated by a dashed line.

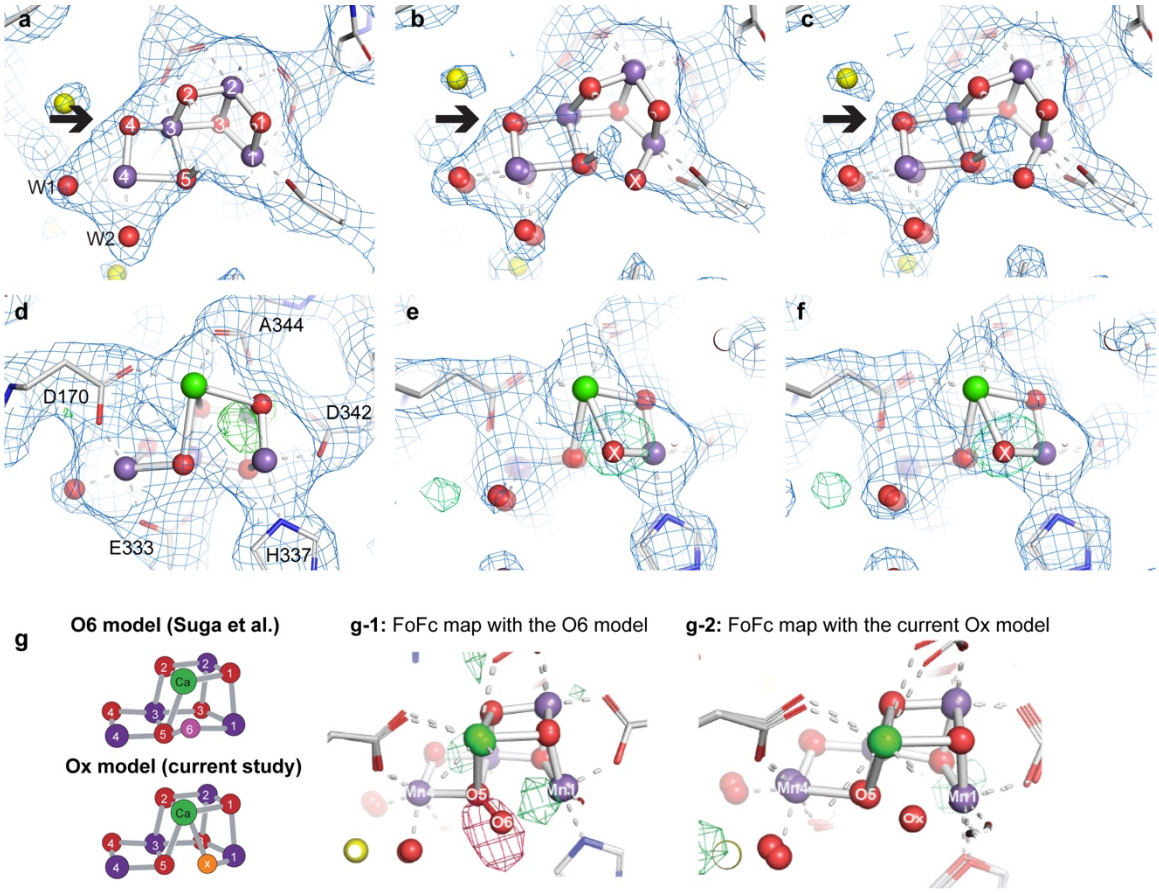

Extended Data Figure 5 | Impact of the data quality on the resolving power of the maps. a-f: The data quality evidenced by 2F state models and $2mF_{obs}$-DF_{calc} maps contoured at 1.5 σ. **a,** 5TIS (2F, 2.25 Å) model and map. Overlays indicate atom numbering in the OEC and the identities of selected coordinating sidechains. **b,** Current 2F model and map cut to 2.25 Å. **c,** Current 2F model and map at the full 2.07 Å resolution. Locations of O4 emerging with improved data quality is indicated by bold arrow. **d,** As **a** from a different angle and with mF_{obs}-DF_{calc} density at 3 σ indicating the lack of sufficient evidence for inserting an additional O atom at a chemically reasonable position. **e-f,** As **b-c** from the same direction as **d** and with mF_{obs}-DF_{calc} density at 3 σ shown to 2.25 and 2.05 Å, respectively, after omitting the inserted Ox atom. Centering of the refined Ox position within the omit density gives clear indication of the position of the inserted water in the S_3 state with the current, higher-quality data, even when artificially cut to the same resolution as the previous dataset. **g,** mF_{obs}-DF_{calc} maps of the 2F data that compare the O6 model from Suga *et al.*[9] and the Ox model from the current study. Map shows the mF_{obs}-DF_{calc} density calculated with our current 2F data and our model adding the O6 position of Suga *et al.*[9] (with the occupancy of 0.7 and B-factor of 30) (**g-1**), and with our Ox model (**g-2**). We see clearly a positive density for the missing Ox and a negative density at the O6 position in g-1. Schematics of the O6 and Ox S_3 models are shown on the left.

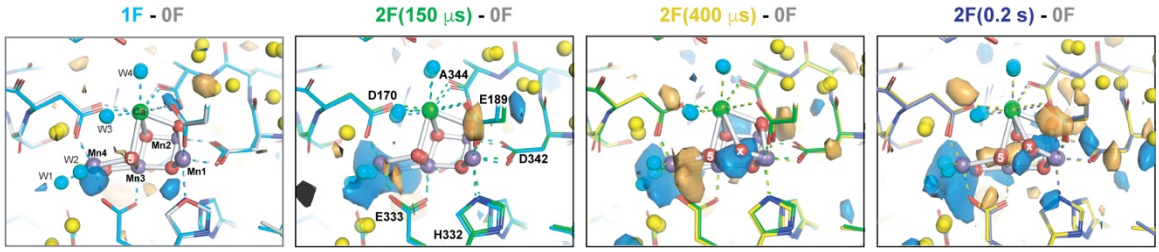

Extended Data Figure 6 | Isomorphous difference maps in the 2nd monomer at the OEC. Isomorphous difference density OEC sites in monomer 'a'. F_{obs}-F_{obs} difference densities between the various illuminated states and the 0F data are contoured at +3σ (blue) and -3σ (orange), the model for the 0F data is shown in light grey whereas carbons are colored in the models for 1F (cyan), 2F(150 µs) (green), 2F(400 µs) (yellow) and 2F(0.2 s) (blue).

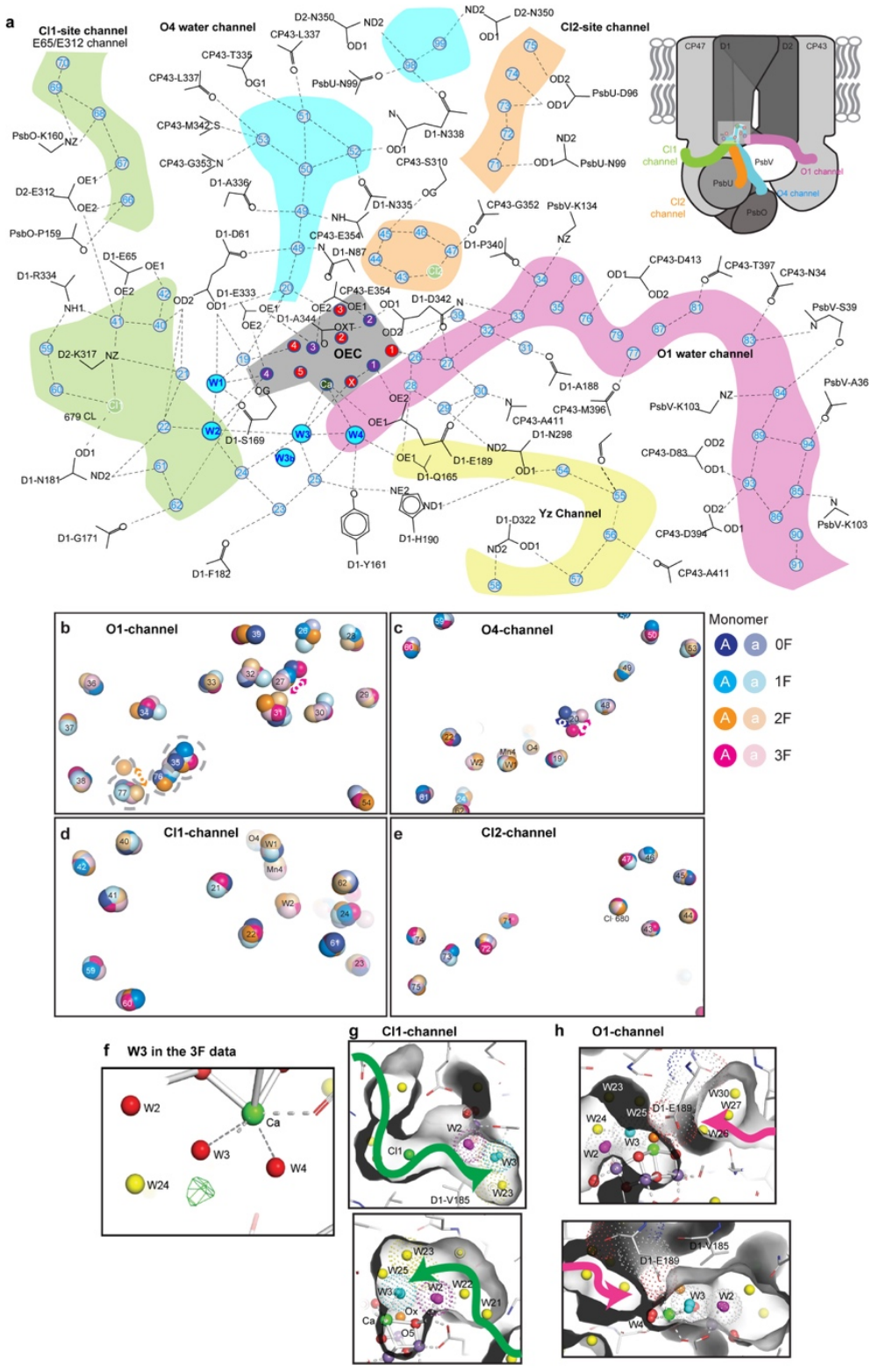

Extended Data Figure 7 | Water environment of the OEC. a, Extended schematic of the hydrogen bonding network connecting the OEC to the solvent-exposed surface of PS

II and identification of several channels for either possible water movement or proton transfer. The scheme in the top right shows the locations of four selected channels in the PS II monomer. **b-e)** Movements within the water networks across monomers. Colored spheres are shown for each ordered water or chloride ion across the four metastable states, 0F through 3F, and for both monomers, with the stronger color matching the first (A) monomer and the lighter color matching the second (a) monomer. For ordered solvent, residue number is shown; for OEC atoms, the atom identifier is shown; and for the Cl2 site, the Cl^- 680 label is shown. **b,** The O1 water chain. Positional disagreement between monomers is visible especially near waters 77 (2F) and 27 (3F) and is on the same scale as changes between illuminated states, both of which may indicate a more dynamic water channel. **c,** The O4 water chain. With the notable exception of water 20, most water positions are stable across monomers and illuminated states. Water 20 is highly unstable in position in the two states (0F, 3F) in which it is modeled, and there is not sufficient density in the remaining states to model a water 20 position. **d,** The Cl1 site water channel with no notable movements. **e,** the Cl2 site water channel with no notable movements. **f,** Indication of a split position of W3 in the S_0 state. mF_{obs}-DF_{calc} difference density (green mesh) in the 3F state suggests an alternate position near W3 (noted as W3b in Fig. 4d). **g,h,** Possible access to W3/Ox side from the Cl1 or the O1 channel. The surface of the protein is shown in grey to visualize the extend of the cavities around the OEC and Van der Waals radii are indicated for selected residues/atoms by dotted spheres. Shown are two different views for each channel. The direction of the Cl1 channel is indicated by a green arrow, the O1 channel by a pink arrow. Water W2 is shown in purple, W3 in cyan and Ox in orange. Yellow spheres indicate other waters. Mn are shown in magenta, other bridging oxygens as red spheres.

Extended Data Table 1 | Merging and refinement statistics for (a) the refined datasets including all lattices or (b) for the additional datasets containing only lattices with unit cells within 1% of the target unit cell.

a

	0F	1F	2F (150 µs)	2F (400 µs)	2F‡	3F‡
Resolution range refined (Å)	30.552 - 2.05	30.427 - 2.08	30.783 - 2.5	30.851 - 2.2	30.578 - 2.07	31.005 - 2.04
Resolution range upper bin (Å)	2.085 - 2.05	2.116 - 2.08	2.543 - 2.5	2.238 - 2.2	2.106 - 2.07	2.075 - 2.04
Wavelength (Å)	1.303	1.303	1.301	1.301	1.303	1.303
Space group	$P2_12_12_1$	$P2_12_12_1$	$P2_12_12_1$	$P2_12_12_1$	$P2_12_12_1$	$P2_12_12_1$
Unit cell parameters (Å)	a=116.9 b=221.4 c=308.7	a=116.8 b=220.9 c=307.0	a=117.6 b=222.7 c=309.1	a=117.7 b=222.6 c=308.5	a=117.0 b=221.5 c=308.3	a=116.7 b=221.2 c=307.6
Images merged	30366	23744	4231	13072	24481	25134
Unique reflections	508701	487161	281837	412258	494189	516201
(upper bin)	(25202)	(24128)	(13902)	(20410)	(24482)	(25594)
Completeness	99.95%	99.95%	99.92%	99.94%	99.95%	99.95%
(upper bin)	(99.81%)	(99.78%)	(99.96%)	(99.91%)	(99.87%)	(99.86%)
$CC_{1/2}$	98.7%	97.5%	93.8%	96.0%	98.2%	98.6%
(upper bin)	(1.8%)	(1.3%)	(6.8%)	(0.6%)	(2.1%)	(0.8%)
Multiplicity	186.8	160.1	45.4	98.4	156.8	170.7
(upper bin)	(9.0)	(8.4)	(9.2)	(9.8)	(9.6)	(9.3)
Pred. multiplicity*	458.3	383.1	88.2	272.3	375.1	413.0
(upper bin)	(360.4)	(301.8)	(66.6)	(209.9)	(291.9)	(318.6)
$I/\sigma_{Ha14}(I)^{\dagger}$	16.6	15.0	11.1	10.6	15.5	17.0
(upper bin)	(0.5)	(0.5)	(1.0)	(0.7)	(0.6)	(0.6)
Wilson B-factor	26.8	27.1	35.5	27.4	27.3	27.1
R-factor	18.48%	18.90%	16.69%	19.33%	18.44%	18.64%
R-free	23.99%	24.56%	24.60%	26.39%	24.75%	24.85%
Number of atoms	103732	103728	103713	103719	105764	105761
Number non-hydrogen atoms	52203	52199	52188	52194	53286	53283
Ligands	186	186	186	186	188	188
Waters	2021	2017	2012	2016	2015	2010
Protein residues	5306	5306	5306	5306	5306	5306
RMS (bonds)	0.014	0.015	0.015	0.016	0.014	0.014
RMS (angles)	1.51	1.53	1.57	1.61	1.52	1.50
Ramachandran favored	96.5%	95.8%	94.8%	95.3%	96.2%	96.3%
Ramachandran outliers	0.31%	0.38%	0.56%	0.38%	0.34%	0.31%
Clashscore	5.4	6.5	6.8	6.3	6.6	6.8
Average B-factor	42.8	44.4	50.3	46.5	43.4	42.3

b

	0F	1F	2F (150 µs)	2F (400 µs)	2F‡	3F‡
Resolution range refined (Å)	30.05 - 2.07	30.04 - 2.13	29.70 - 2.60	29.85 - 2.30	30.18 - 2.09	30.05 - 2.05
Resolution range upper bin (Å)	2.11 - 2.07	2.17 - 2.13	2.65 - 2.60	2.34 - 2.30	2.13 - 2.09	2.09 - 2.05
Wavelength (Å)	1.301	1.301	1.301	1.301	1.301	1.301
Space group	$P2_12_12_1$	$P2_12_12_1$	$P2_12_12_1$	$P2_12_12_1$	$P2_12_12_1$	$P2_12_12_1$
Unit cell parameters (Å)	a=117.6 b=222.8 c=309.7	a=117.6 b=222.8 c=309.7	a=117.6 b=222.8 c=309.7	a=117.6 b=222.8 c=309.7	a=117.6 b=222.8 c=309.7	a=117.6 b=222.8 c=309.7
Images merged	15669	10757	2087	4576	13603	14019
Unique reflections	490658	450643	249070	358519	476797	505050
(upper bin)	(24364)	(22354)	(12358)	(17699)	(23606)	(25047)
Completeness	99.96%	99.95%	99.91%	99.93%	99.96%	99.95%
(upper bin)	(99.98%)	(99.96%)	(99.93%)	(99.93%)	(99.96%)	(99.92%)
$CC_{1/2}$	98.2%	95.6%	92.4%	96.1%	97.7%	98.0%
(upper bin)	(2.1%)	(2.8%)	(6.8%)	(2.9%)	(0.9%)	(0.4%)
Multiplicity	98.5	71.7	28.3	48.3	89.9	101.2
(upper bin)	(11.1)	(10.6)	(9.8)	(10.4)	(11.0)	(10.6)
Pred. multiplicity*	204.8	144.2	41.3	86.3	187.6	210.1
(upper bin)	(153.1)	(107.2)	(29.81)	(62.32)	(139.22)	(154.24)
$I/\sigma_{Ha14}(I)^{\dagger}$	13.3	11.1	11.5	10.6	12.7	14.3
(upper bin)	(0.7)	(0.7)	(1.1)	(0.8)	(0.7)	(0.6)
Wilson B-factor	24.4	24.4	31.8	24.0	24.8	24.9
R-factor	19.18%	19.75%	17.99%	19.82%	19.48%	19.44%
R-free	23.20%	24.43%	23.97%	24.94%	23.93%	23.62%
Number of atoms	52325	52154	50943	51500	52251	52319
Number non-hydrogen atoms	52325	52154	50943	51500	52251	52319
Ligands	187	187	187	187	187	187
Waters	2226	2054	843	1400	2151	2219
Protein residues	5300	5300	5300	5300	5300	5300

RMS (bonds)	0.008	0.009	0.009	0.009	0.008	0.008
RMS (angles)	0.98	1.06	1.08	1.07	0.97	0.97
Ramachandran favored	97.3%	97.1%	96.5%	96.8%	97.6%	97.5%
Ramachandran outliers	0.36%	0.31%	0.38%	0.27%	0.35%	0.27%
Clashscore	5.7	6.7	7.7	7.3	6.0	5.9
Average B-factor	37.6	39.9	44.2	44.4	38.9	38.6

[*]Predictions multiplicity is the multiplicity of all spot predictions matching the indexing solution on a given image, before a per-image resolution cutoff. Multiplicities for datasets merged by the Monte Carlo method (*e.g.* Kupitz *et al.*[65], and Suga *et al.*[9]) without per-image resolution cutoffs are best compared with this metric.

[†]I/sigma calculation by the Hattne 2014 method[46,64].

[‡] For the 2F and 3F data sets a region of 66 amino acids around the OEC was modeled as double conformers to reflect the contribution from the two main S-state species in each of the data sets with contributions of 30%/70% for S_2 and S_3 in the 2F and 40%/60% for S_3 and S_0 in the 3F data sets.

Extended Data Table 2 | Interatomic distances at the OEC in each merged dataset, in each monomer (A/a), in Å.

		0F		1F		2F (150 µs)		2F (400 µs)		2F OEI (S_3)		3F OEC (S_0)	
Distances (Å)		A	a	A	a	A	a	A	a	A	a	A	a
CA1-	MN1	3.41	3.45	3.46	3.38	3.49	3.45	3.47	3.58	3.37	3.37	3.44	3.31
	MN2	3.38	3.38	3.40	3.42	3.40	3.44	3.41	3.39	3.27	3.38	3.45	3.41
	MN3	3.52	3.49	3.54	3.50	3.42	3.53	3.49	3.57	3.52	3.61	3.55	3.52
	MN4	3.77	3.88	3.90	3.90	3.72	3.96	3.84	4.07	3.90	4.11	3.94	4.07
MN1-	MN2	2.77	2.77	2.85	2.77	2.89	2.78	2.86	2.72	2.77	2.73	2.81	2.71
	MN3	3.22	3.26	3.29	3.22	3.38	3.32	3.39	3.35	3.34	3.32	3.30	3.24
	MN4	4.80	4.91	4.84	4.88	5.01	5.05	5.05	5.16	5.01	5.11	4.97	4.98
MN2-	MN3	2.87	2.83	2.86	2.82	2.85	2.83	2.88	2.82	2.85	2.86	2.90	2.82
MN3-	MN4	2.70	2.77	2.70	2.79	2.70	2.84	2.74	2.90	2.70	2.84	2.79	2.91
MN1-	Ox							1.82	1.67	1.78	1.80		
MN4-	O5							2.23	2.28	2.17	2.27		
O5-	Ox							1.84*	1.87*	2.10	2.07		
MN4-	W1	2.18	2.13	2.06	2.17	2.03	1.97	2.37	2.23	2.16	2.10	2.04	2.01
	W2	2.12	2.14	2.13	2.19	2.09	2.37	2.20	2.43	2.11	2.13	2.22	2.22
CA1-	W3	2.53	2.53	2.58	2.63	2.58	2.59	2.52	2.57	2.51	2.58	2.61	2.56
	W3B/C											3.25	4.26
	W4	2.36	2.30	2.37	2.22	2.57	2.37	2.37	2.43	2.30	2.30	2.20	2.29

*The O5-Ox distance in the 2F(400µs) dataset is shorter compared to the 2F dataset as for this data set we did not model two configurations for the OEC. Hence, the O5 position that is used to measure the O5-Ox distance is definitely influenced by the contribution of O5 in the S_2 state (closer to Mn1) and only partly by O5 in the S_3 state (longer Mn1-O5 distance).

Extended Data Table 3 | Channel nomenclature in the literature. Summary of the correspondence of the multiple names used for identifying the water and proton channels in PS II.

This work	Ho and Styring[68]	Vassiliev[69]	Murray[70]	Gabdulkhakov[71]	Umena[72]	Sakashita[73]
O1 channel	large channel	4.A	*channel ii*	B1		O1-water chain
O4 channel	narrow channel	2		E, F		O4-water chain
Cl1 channel	broad channel	1	*channel iii*	D	4.b	E65/E312 channel
Cl2 channel					4.c	

32. Hellmich, J. *et al.* Native-like photosystem II superstructure at 2.44 Å resolution through detergent extraction from the protein crystal. *Structure* **22**, 1607-1615 (2014).

33. Ibrahim, M. *et al.* Improvements in serial femtosecond crystallography of photosystem II by optimizing crystal uniformity using microseeding procedures. *Struct. Dyn.* **2**, 041705 (2015).

34. Guskov, A. *et al.* Cyanobacterial photosystem II at 2.9 Å resolution and the role of quinones, lipids, channels and chloride. *Nat. Struct. Mol. Biol.* **16**, 334-342 (2009).

35. Krivanek, R., Kern, J., Zouni, A., Dau, H. & Haumann, M. Spare quinones in the Q_B cavity of crystallized photosystem II of thermosynechococcus elongatus. *Biochim. Biophys. Acta-Bioenerg.* **1767**, 520-527 (2007).

36. Fransson, T. *et al.* X-ray emission spectroscopy as an *in situ* diagnostic tool for X-ray crystallography. *Biochemistry*, DOI: 10.1021/acs.biochem.8b00325, (2018).

37. Fuller, F. D. *et al.* Drop-on-demand sample delivery for studying biocatalysts in action at XFELs *Nat. Methods* **14**, 443-449 (2017).

38. Kern, J. *et al.* Taking snapshots of photosynthetic water oxidation using femtosecond X-ray diffraction and spectroscopy. *Nat. Commun.* **5**, 4371 (2014).

39. Yano, J. *et al.* Light-Dependent Production of Dioxygen in Photosynthesis, in *Sustaining Life on Planet Earth: Metalloenzymes Mastering Dioxygen and Other*

Chewy Gases, Metal Ions in Life Sciences (eds P. M. H. Kroneck & M. E. Sosa Torres) 13-43 (Springer International Publishing, 2015).

40. Beckmann, K., Messinger, J., Badger, M. R., Wydrzynski, T. & Hillier, W. On-line mass spectrometry: Membrane inlet sampling. *Photosynth. Res.* **102**, 511-522 (2009).

41. Emma, P. *et al.* First lasing and operation of an Ångstrom-wavelength free-electron laser. *Nat. Photonics* **4**, 641-647 (2010).

42. Boutet, S., Cohen, A. E. & Wakatsuki, S. The new macromolecular femtosecond crystallography (MFX) instrument at LCLS. *Synchr. Rad. News* **29**, 23-28 (2016).

43. Sauter, N. K. XFEL diffraction: Developing processing methods to optimize data quality. *J. Synchr. Rad.* **22**, 239-248 (2015).

44. Winter, G. *et al.* DIALS: Implementation and evaluation of a new integration package. *Acta Cryst. D* **74**, 85-97 (2018).

45. Sauter, N. K., Hattne, J., Grosse-Kunstleve, R. W. & Echols, N. New python-based methods for data processing. *Acta Cryst. D* **69**, 1274-1282. (2013).

46. Hattne, J. *et al.* Accurate macromolecular structures using minimal measurements from X-ray free-electron lasers. *Nat. Methods* **11**, 545-548 (2014).

47. Sauter, N. K. *et al.* Improved crystal orientation and physical properties from single-shot XFEL stills. *Acta Cryst. D* **70**, 3299-3309 (2014).

48. Waterman, D. G. *et al.* Diffraction-geometry refinement in the DIALS framework. *Acta Cryst. D* **72**, 558-575 (2016).

49. Zeldin, O. B. *et al.* Data exploration toolkit for serial diffraction experiments. *Acta Cryst. D* **71**, 352-356 (2015).

50. Andrews, L. C. & Bernstein, H. J. The geometry of Niggli reduction: Bgaol - embedding Niggli reduction and analysis of boundaries. *J. Appl. Cryst.* **47**, 1477-1477 (2014).

51. Suga, M. *et al.* Native structure of photosystem II at 1.95 Å resolution viewed by femtosecond X-ray pulses. *Nature* **517**, 99-103 (2015).

52. Uervirojnangkoorn, M. *et al.* Enabling X-ray free electron laser crystallography for challenging biological systems from a limited number of crystals. *eLife* **4**, 2050-2084 (2015).

53. Lyubimov, A. Y. *et al.* Advances in X-ray free electron laser (XFEL) diffraction data processing applied to the crystal structure of the synaptotagmin-1/snare complex. *eLife* **5**, e18740 (2016).

54. Adams, P. D. *et al.* Phenix: A comprehensive python-based system for macromolecular structure solution. *Acta Cryst. D* **66**, 213-221 (2010).

55. Afonine, P. V. *et al.* Towards automated crystallographic structure refinement with phenix.Refine. *Acta Cryst. D* **68**, 352-367 (2012).

56. Emsley, P., Lohkamp, B., Scott, W. G. & Cowtan, K. Features and development of coot. *Acta Cryst. D* **66**, 486-501 (2010).

57. Wieghardt, K. The active-sites in manganese-containing metalloproteins and inorganic model complexes. *Angew. Chem. Int. Edit. Engl.* **28**, 1153-1172 (1989).

58. Cinco, R. M. *et al.* Comparison of the manganese cluster in oxygen-evolving photosystem II with distorted cubane manganese compounds through X-ray absorption spectroscopy. *Inorg. Chem.* **38**, 5988-5998 (1999).

59. Mukhopadhyay, S., Mandal, S. K., Bhaduri, S. & Armstrong, W. H. Manganese clusters with relevance to photosystem II. *Chem. Revs.* **104**, 3981-4026 (2004).

60. Law, N. A., Caudle, M. T. & Pecoraro, V. L. Manganese redox enzymes and model systems: Properties, structures, and reactivity, in *Advances in Inorganic Chemistry* Vol. 46 305-440 (1999).

61. Tsui, E. Y., Kanady, J. S. & Agapie, T. Synthetic cluster models of biological and heterogeneous manganese catalysts for O_2 evolution. *Inorg. Chem.* **52**, 13833-13848 (2013).

62. Schrödinger LLC. The pymol molecular graphics system, version 1.8. (2015).

63. Lang, P. T., Holton, J. M., Fraser, J. S. & Alber, T. Protein structural ensembles are revealed by redefining X-ray electron density noise. *Proc. Natl. Acad. Sci. U. S. A.* **111**, 237-242 (2014).

64. Brewster, A. S. *et al.* Improving signal strength in serial crystallography with DIALS geometry refinement. *Acta Cryst. D*, In Press (2018).

65. Kupitz, C. *et al.* Serial time-resolved crystallography of photosystem II using a femtosecond X-ray laser. *Nature* **513**, 261-265 (2014).

66. Ho, F. M. & Styring, S. Access channels and methanol binding site to the $CaMn_4$ cluster in photosystem II based on solvent accessibility simulations, with implications for substrate water access. *Biochim. Biophys. Acta Bioenerg.* **1777**, 140-153 (2008).

67. Vassiliev, S., Zaraiskaya, T. & Bruce, D. Exploring the energetics of water permeation in photosystem II by multiple steered molecular dynamics simulations. *Biochim. Biophys. Acta Bioenerg.* **1817**, 1671-1678 (2012).

68. Murray, J. W. & Barber, J. Structural characteristics of channels and pathways in photosystem II including the identification of an oxygen channel. *J. Struct. Biol.* **159**, 228-237 (2007).

69. Gabdulkhakov, A. *et al.* Probing the accessibility of the Mn_4Ca cluster in photosystem II: Channels calculation, noble gas derivatization, and cocrystallization with DMSO. *Structure* **17**, 1223-1234 (2009).

70. Umena, Y., Kawakami, K., Shen, J.-R. & Kamiya, N. Crystal structure of oxygen-evolving photosystem II at a resolution of 1.9 Å. *Nature* **473**, 55-60 (2011)

71. Sakashita, N., Watanabe, H. C., Ikeda, T. & Ishikita, H. Structurally conserved channels in cyanobacterial and plant photosystem II. *Photosynth. Res.* **133**, 75-85 (2017).